

**AEDC-TR-83-33**

c.2



**Design and Initial Operational  
Characteristics of a Shock Tube/  
Raman Scattering Calibration System**

J. W. L. Lewis, G. A. Kroeger, and M. S. Smith  
Calspan Field Services, Inc.

September 1983

Final Report for Period October 1, 1981 – September 30, 1982

Property of U. S. Air Force  
AEDC LIBRARY  
F40600-81-C-0004

Approved for public release; distribution unlimited.

**TECHNICAL REPORTS  
FILE COPY**

**ARNOLD ENGINEERING DEVELOPMENT CENTER  
ARNOLD AIR FORCE STATION, TENNESSEE  
AIR FORCE SYSTEMS COMMAND  
UNITED STATES AIR FORCE**

## NOTICES

When U. S. Government drawings, specifications, or other data are used for any purpose other than a definitely related Government procurement operation, the Government thereby incurs no responsibility nor any obligation whatsoever, and the fact that the government may have formulated, furnished, or in any way supplied the said drawings, specifications, or other data, is not to be regarded by implication or otherwise, or in any manner licensing the holder or any other person or corporation, or conveying any rights or permission to manufacture, use, or sell any patented invention that may in any way be related thereto.

Qualified users may obtain copies of this report from the Defense Technical Information Center.

References to named commercial products in this report are not to be considered in any sense as an endorsement of the product by the United States Air Force or the Government.

This report has been reviewed by the Office of Public Affairs (PA) and is releasable to the National Technical Information Service (NTIS). At NTIS, it will be available to the general public, including foreign nations.

## APPROVAL STATEMENT

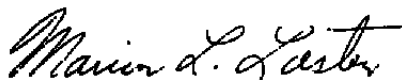
This report has been reviewed and approved.



MARSHALL K. KINGERY  
Directorate of Technology  
Deputy for Operations

Approved for publication:

FOR THE COMMANDER



MARION L. LASTER  
Director of Technology  
Deputy for Operations

## UNCLASSIFIED

SECURITY CLASSIFICATION OF THIS PAGE (When Data Entered)

REPORT DOCUMENTATION PAGE		READ INSTRUCTIONS BEFORE COMPLETING FORM
1. REPORT NUMBER AEDC-TR-83-33	2. GOVT ACCESSION NO.	3. RECIPIENT'S CATALOG NUMBER
4. TITLE (and Subtitle) THE DESIGN AND INITIAL OPERATIONAL CHARACTERISTICS OF A SHOCK TUBE-RAMAN SCATTERING CALIBRATION SYSTEM		5. TYPE OF REPORT & PERIOD COVERED Final Report - Oct. 1, 1981 - Sept. 30, 1982
		6. PERFORMING ORG. REPORT NUMBER
7. AUTHOR(s) J. W. L. Lewis, G. A. Kroeger, and M. S. Smith, Calspan Field Services, Inc. /AEDC Division		8. CONTRACT OR GRANT NUMBER(s)
9. PERFORMING ORGANIZATION NAME AND ADDRESS Arnold Engineering Development Center/DOT Air Force Systems Command Arnold Air Force Station, TN 37389		10. PROGRAM ELEMENT, PROJECT, TASK AREA & WORK UNIT NUMBERS  Program Element 65807F
11. CONTROLLING OFFICE NAME AND ADDRESS Arnold Engineering Development Center/DOS Air Force Systems Command Arnold Air Force Station, TN 37389		12. REPORT DATE September 1983
		13. NUMBER OF PAGES 55
14. MONITORING AGENCY NAME & ADDRESS (if different from Controlling Office)		15. SECURITY CLASS. (of this report) UNCLASSIFIED
		15a. DECLASSIFICATION/DOWNGRADING SCHEDULE N/A
16. DISTRIBUTION STATEMENT (of this Report)  Approved for public release; distribution unlimited.		
17. DISTRIBUTION STATEMENT (of the abstract entered in Block 20, if different from Report)		
18. SUPPLEMENTARY NOTES  Available in Defense Technical Information Center (DTIC).		
19. KEY WORDS (Continue on reverse side if necessary and identify by block number) shock tubes Raman spectra gases heat transfer lasers		
20. ABSTRACT (Continue on reverse side if necessary and identify by block number) A shock tube system has been designed and constructed to provide a high-temperature, local thermal equilibrium gas sample for the determination of Raman scattering cross sections. The shock tube was designed for operation over the temperature (T) range of $800 \leq T \leq 4000$ K and the number density (n) range of $0.2 \leq n \leq 2.1$ amagat. The fabricated steel shock tube was 6.98 m long with a 6.35-cm inner diameter; the driven/driver section length ratio		

## 20. ABSTRACT (Continued)

was 1.88. The initial demonstration of a laser Raman-shock tube system for high-temperature cross section and calibration measurements was accomplished. The incident Mach number range of 4 to 5 was studied with the driver gas and  $N_2$  as the driven species using a seamless steel shock tube and the same tube which was retrofitted with a stainless steel tube liner. The Raman spectra obtained with the seamless steel tube revealed excessively high contributions to the scattering signal due to effects of rust particles which had been scrubbed from the tube wall. Upon insertion of the stainless steel liner, these effects were reduced to small corrections to the Raman signal. Vibrational Raman spectra of shock-heated  $N_2$  were acquired using a frequency-doubled ruby laser, spectrometer dispersion, and a single PMT detection channel. The results were acquired at two wavelengths of the vibrational Raman Stokes band, and  $T_v$  was determined. The results of these measurements yielded a mean vibrational temperature  $\bar{T}_v = 2110 \pm 220$  K. Heat-transfer gauges were used to determine the shock speed  $W_s$  and incident Mach number  $M_1$  which was found to be  $4.96 \pm 0.04$ . The incident gas temperature corresponding to  $M_1 = 4.96$  was approximately  $T_2 = 1600$  K, and the discrepancy between  $T_2$  and  $\bar{T}_v$  is attributed to observation in the early portion of the reflected shock region rather than the latter phase of the incident shock.

## **PREFACE**

The work reported herein was sponsored by the Arnold Engineering Development Center (AEDC), Air Force Systems Command (AFSC) for the Directorate of Technology (DOT), under Program Element 65807F. The results were obtained by Calspan Field Services, Inc./AEDC Division, operating contractor for the Aerospace Flight Dynamics testing at AEDC, AFSC, Arnold Air Force Station, Tennessee under AEDC Project No. D200PW (P32M-C4). The Air Force Project Manager was 2nd Lt. Steve Lehr.

## CONTENTS

1.0	INTRODUCTION .....	5
2.0	DESIGN CONSIDERATIONS .....	8
2.1	Ideal Shock Tube Performance Predictions .....	8
2.2	Non-Ideal Effects of Shock Tube Operation .....	13
3.0	SHOCK TUBE SYSTEM .....	18
3.1	Shock Tube Configuration .....	18
3.2	Conventional Instrumentation .....	20
3.3	Laser System and Observation Cell .....	21
4.0	RESULTS AND CONCLUSIONS .....	22
4.1	Results .....	22
4.2	Conclusions .....	25
	REFERENCES .....	26

## ILLUSTRATIONS

<u>Figure</u>		<u>Page</u>
1.	Typical Shock Tube Configuration for Reflected Mode Operation .....	29
2.	Flow Diagram of Shock Tube Regions at Time $t$ after Diaphragm Rupture .....	30
3.	Ideal Gas Temperature, Pressure, and Number Density Ratios for Nitrogen Shocks .....	31
4.	Ideal Gas Temperature and Number Density Ratios for Nitrogen Reflected Shocks .....	32
5.	Shock Tube Time-Position Loci Diagram .....	33
6.	Incident Shock Flow Time for $N_2$ Versus Mach Number $M_1$ .....	34
7.	Reflected Flow Time versus Driver and Driven Tube Lengths at Mach 3 .....	35
8.	Reflected Flow Time versus Mach Number or Driver and Driven Lengths .....	36
9.	Boundary Layer in Shocked Gas .....	37
10.	Trajectory Diagram .....	38
11.	Particle Time as a Function of Shock Distance .....	39
12.	Variation of Temperature Ratio $T_{2c}/T_{2s}$ with Mach Number $M_s$ .....	40

13. Variation of Number Density Ratio  $n_{2c}/n_{2s}$   
with Mach Number  $M_s$  ..... 41

14. Sketch of Variation of Shocked Gas Temperatures  
with Distance  $l$  into Region 2 ..... 42

15. Shock Tube and Mounting Installation ..... 43

16. Platinum Heat Transfer Gauge Insert ..... 44

17. Shock Tube Test Cell, Laser, and Spectrometer Configuration ..... 45

18. Pressure Ratio  $P_4/P_1$  versus Shock Speed  $W_s$  ..... 46

19. Shock Front Time - Distance Results ..... 47

20. Raman Spectral Profile for  $N_2$  ..... 48

21. Variation of Raman Signal Levels with  
Vibrational Temperature  $T_v$  ..... 49

22. Ratio  $R_v$  of Raman Signals versus  $T_v$  ..... 50

23. Oscilloscope Traces of Raman Signals  $S(\lambda_0)$  and  $S(\lambda_1)$  ..... 51

**TABLE**

1. Conventional Instrumentation ..... 52

NOMENCLATURE ..... 53

## 1.0 INTRODUCTION

The use of laser scattering techniques such as spontaneous and nonlinear Raman scattering for diagnostics of gas flow-field and combustion environments has been successfully demonstrated previously by various groups. This particular panoply of techniques provides the capability to perform local, time-resolved measurements of the number density of individual species as well as the energy distribution or enthalpy of the rotational and the individual vibrational modes of molecular species. The previous applications of these measurement methods have included measurements of the free-stream flow properties of nozzles (Refs. 1 and 2) and orifice sources (Ref. 3) as well as studies of the boundary and shock layers of an aerodynamic model (Refs. 4 and 5), measurements of the exit plane properties of monopropellant liquid rocket exhaust plumes (Ref. 6) and a turbulent, two-stream H<sub>2</sub>-air combustion flow field (Ref. 7), and, more recently, spontaneous and nonlinear Raman scattering studies of both spark ignition engines (Refs. 8 and 9) and compression ignition engines (Ref. 10). The success of these diverse applications has been such that the focus of research and development in several areas has shifted from the question of feasibility of the techniques to that of the ultimate, but practical, uncertainty of the methods of measurement. To appreciate the question of ultimate uncertainty of the measurement, it is helpful to recall the basic equation which relates the scattered signal S to the power P<sub>o</sub> of the laser of frequency ν<sub>o</sub>, the subtended collection optics solid angle (ΔΩ), the total number density (n<sub>T</sub>) of the scattering species and the thermally-averaged differential cross section (dσ/dΩ) for the transition of interest. Although the signal-to-noise ratio is the pertinent parameter, for the purpose of this work it is sufficient to note that

$$S = n_T \left( \frac{d\sigma}{d\Omega} \right) \times \left( \frac{P_o}{h\nu_o} \right) \times \Delta\Omega \times \ell$$

from which it is seen that S varies directly with the differential cross section dσ/dΩ. Therefore, knowledge of dσ/dΩ for the species is essential for quantitative determinations of density n and rotational and vibrational temperatures T<sub>R</sub> and T<sub>V</sub>, respectively.

If the gas sample of interest can be provided for a laboratory calibration for which the conditions can be varied to span the range of parameters of the unknown gas sample, it is a simple matter to perform an *in situ* calibration and to use theoretical predictions, which have been verified by the laboratory calibrations, to determine the desired properties of the gas. However, it is not uncommon that the properties of the unknown gas sample cannot be spanned by conventional laboratory studies, and, consequently, the theoretical predictions are unverified. For simple and well-understood species such as N<sub>2</sub> and H<sub>2</sub> such an extrapolation is normally justifiable. However, with increased complexity of the molecular species arise difficulties in the interpretation of spectral intensities. These difficulties are

typified by complex overtone spectra and intramolecular perturbations such as the Fermi resonance phenomenon. For such molecular species, at the high vibrational temperatures encountered in various applications of spontaneous and coherent Raman scattering, these uncertainties in knowledge of the spectral intensity distributions are reflected as uncertainties in the Raman cross sections and result in uncertainties in the measured values of species density and temperatures. Therefore, calibrations or cross section measurements are required for these species over the temperature range of interest for the required applications.

The temperature range of interest for the various applications of Raman scattering is quite broad and spans the nominal range of 20-3000 K. Calibration and cross section measurements for the 20 to  $\approx$  1200 K range can be performed using a combination of experimental methods including expansion flow fields, cryogenically cooled gases, resistance-heated furnaces, and compression ignition engines which are operated in a non-combusting mode (Ref. 10). However, for the higher temperature range (1200-3000 K) the choices are less abundant. Even though a variety of techniques exists to heat gases, for cross section measurements it is essential that the gas be in a state of local thermal equilibrium (LTE), at least with respect to the modes of molecular motion involved in the Raman process. Because of this requirement, the available methods for providing the LTE gas sample are reduced to essentially two: the flat-flame burner (Ref. 11) and the shock tube (Ref. 12). The burner method has been used successfully by Lapp and co-workers (Ref. 13) for a variety of cross section measurements of gases which occur normally as a result of the combustion process. However, there are features of this approach which contraindicate its use for general cross section measurements. First, the temperature range of the flat-flame burner is inadequate because 3000 K cannot be obtained routinely. Second, unless the species of interest is a normal combustion product of the flame reactants, the selection of which determines the flame temperature, the species must be injected into the flame with a concentration sufficient for the cross section measurement. However, this very injection can alter significantly the properties of the flame, thereby invalidating its status as a standard. Additional flame calibrations will then be required for each concentration level of the injected species, and the precision of the cross section measurement is degraded. Moreover, it is possible that the injected species will experience chemical reactions with the flame species, further complicating the task. Finally, for a burner of reasonable size, the magnitude of the spatial gradients of the flame properties is a serious consideration, and, quite likely, these gradients result in severe restrictions in the experimental design of the cross section measurements.

The shock tube alternative to the use of combustion flame gas sources is a relatively simple laboratory tool for the production of high-temperature, LTE gas samples; a sketch of a typical shock tube is shown in Fig. 1. For ideal operation, the desired high-temperature gas

sample can be provided over a range of temperatures by simply varying the ratio of the initial driver-driven gas pressures (Ref. 12). Also, the shocked gas density can be varied while the shocked gas temperature is held constant by simultaneously varying the driven gas pressure and the ratio of the driver-driven gas pressures. Flexibility in the experimental design is achieved by observation of the even greater temperature and gas density values of the reflected shock region. Additional advantages of the technique include the capability of operation of the shock tube with the species of interest as a pure gas sample, unlike the combustion source, and, using a reasonable diameter shock tube, measurements can be performed, in principle, with an LTE gas sample with small spatial gradients. Therefore, as will be shown in the following section, the shock tube provides a method of spanning both the temperature and number density ranges required for the various cross section studies.

The major disadvantage of the use of shock tubes for cross section measurements has been the comparatively short run times and data acquisition periods available for the measurement. For example, 10-50  $\mu$ sec represents a typical interval of time available for measurements in the incident shock region; operation of the shock tube in the reflected mode can increase this interval by over an order of magnitude (Ref. 12). Regardless of the mode of operation of the shock tube, data acquisition times of 50  $\mu$ sec - 1 msec are quite short in comparison to the time available for continuous combustion sources. Clearly, the availability of pulsed laser sources lessens the severity of the short run-time disadvantage, and the use of a Q-switched laser source with a nominal 10-nsec pulse width easily achieves the required temporal resolution. However, the flow duration disadvantage is not eliminated because of the methods normally employed for spectral dispersion and subsequent detection. Specifically, detection and registration are desired for the spectrally resolved scattered radiation for broad wavelength regions, but practical requirements for the minimum acceptable signal-to-noise ratio (S/N) of Raman scattering and the typical pulse duration and repetition rate of the laser source prevent the use of rapid-scan spectrometers. The utilization of single or multiple photomultiplier tubes (PMT) with a fixed wavelength setting of the spectrometer is, of course, possible (Ref. 10). However, using this approach to cover the desired broad spectral region and to simultaneously provide the spectral resolution necessary for the cross section measurements requires the use of multiple shock tube-laser source firings in conjunction with variation in the central wavelength of the spectrometer. Consequently, because of the shot-to-shot variations in both laser and shock tube parameters, the resulting cross section data can be expected to exhibit larger than necessary experimental uncertainty values. As a result of these anticipated difficulties, the use of shock tube flows for Raman scattering studies has not been actively pursued.

However, the relatively recent improvement and development of image intensifier detectors provides exactly the needed detection method. With this type of detector, both broad-band and high spectral resolution detection are possible for 10-nsec pulse sources.

This development now provides the capability of cross section measurements, using single laser firings, thus removing a major obstacle in the use of the shock tube for cross section measurements.

Having discussed the general rationale for the use of the shock tube for cross section measurements and having shown that recent instrumentation developments have eliminated the major objections to the use of this tool, it is necessary to consider both the design criteria for such a shock tube system and to investigate the known problems of operation of a practical shock tube system. Subsequent sections of this report will specify the operational requirements and design criteria of the shock tube and the considerations of first-order corrections for real-gas effects, such as shock wave attenuation, boundary-layer formation, and degradation of the ideal run time. Additionally, a description will be presented of the shock tube system which was fabricated to satisfy these requirements. Finally, the laser scattering system which was assembled to perform the Raman scattering measurements will be described, and preliminary results of vibrational Raman scattering measurements of shock heated N<sub>2</sub> will be presented.

## 2.0 DESIGN CONSIDERATIONS

### 2.1 IDEAL SHOCK TUBE PERFORMANCE PREDICTIONS

As a brief review of the operation of the shock tube, Fig. 2 sketches the trajectory of an ideal shock wave and defines the various regions of the gas shock flow field. As seen in the depiction of the pressure wave, the parameter subscripts denote the following regions of the shock tube:

Subscripts	Region
1	Driven gas
2	Incident shock wave region between shock front and contact surface
3	Region between contact surface and rarefaction wave
4	Driver gas
5	Reflected shock region

The quantitative description of the shock wave is given by the following relations (Ref. 12).

Incident shock pressure ratio:

$$\frac{P_2}{P_1} = \frac{[2\gamma M_1^2 - (\gamma - 1)]}{(\gamma + 1)} \quad (1)$$

Incident shock temperature ratio:

$$\frac{T_2}{T_1} = \left[ \gamma M_1^2 - \frac{(\gamma - 1)}{2} \right] \times \frac{\left[ \frac{(\gamma - 1)}{2} M_1^2 + 1 \right]}{\left[ \frac{(\gamma + 1)}{2} M_1 \right]^2} \quad (2)$$

Incident shock mass and number density ratios:

$$\frac{\rho_2}{\rho_1} = \frac{n_2}{n_1} = \frac{(\gamma + 1) M_1^2}{[(\gamma - 1) M_1^2 - 2]} \quad (3)$$

Incident shock Mach number:

$$M_1 = \frac{W_s}{a_1} \quad (4)$$

Reflected shock pressure ratio:

$$\frac{P_5}{P_1} = \left\{ \frac{[2\gamma M_1^2 - (\gamma - 1)]}{(\gamma + 1)} \right\} \left\{ \frac{[(3\gamma - 1)M_1^2 - 2(\gamma - 1)]}{[(\gamma - 1)M_1^2 + 2]} \right\} \quad (5)$$

Reflected shock temperature ratio:

$$\frac{T_5}{T_1} = \frac{\left\{ 2(\gamma - 1)M_1^2 + (3 - \gamma) \right\} \left\{ (3\gamma - 1)M_1^2 - 2(\gamma - 1) \right\}}{[(\gamma + 1)M_1]^2} \quad (6)$$

$$\frac{P_5}{P_1} = \frac{n_5}{n_1} = \left( \frac{P_5}{P_1} \right) \left( \frac{T_5}{T_1} \right) \quad (7)$$

Figure 3 shows the variation of  $P_2/P_1$ ,  $T_2/T_1$ ,  $n_2/n_1$  with incident Mach number  $M_1$  and initial pressure ratio  $P_4/P_1$ . Figure 4 shows a similar variation for  $T_5/T_1$  and  $n_5/n_1$  with the ratio  $P_4/P_1$ . For these calculations it has been assumed that  $N_2$  and He are the driven and driver gases, respectively, and that the initial temperatures of the driven and driver gases are

identical. Further, for  $N_2$  it has been assumed that the specific heat ratio  $\gamma = 1.40$ ; i.e., real-gas effects are neglected. From Fig. 3 it is seen that for an initial pressure ratio  $P_4/P_1 \approx 200$  one achieves an incident shock Mach number  $M_1 \approx 4.1$ , temperature ratio  $T_2/T_1 \approx 4.2$  and a density ratio  $n_2/n_1 \approx 4.6$ . Therefore, for  $T_1 = 300$  K and  $n_1 = 0.286$  amagat, the incident shock wave values are  $T_2 = 1260$  K and  $n_2 = 1.3$  amagat. Obviously, smaller ratios of  $P_4/P_1$  produce correspondingly lower values of  $T_2$  and  $n_2$ . If the reflected shock wave is observed, from Fig. 4 it is seen that, for the above case,  $T_5 = 2300$  K and  $n_5 = 4.1$  amagat. Consequently, from the results of these simple computations and the results of Figs. 3 and 4, one sees that it is possible to produce a wide range of values of  $n$  and  $T$  by varying the ratio  $P_4/P_1$  and consequently, the incident shock Mach number  $M_1$ .

For Raman scattering cross section measurements, it was desired to produce an LTE gas sample for which, in the shocked gas region,  $n \leq 10^{19}$  cc $^{-1}$  and  $500 \leq T \leq 3000$  K. Further, the pressure  $P_4$  required to produce the shock waves was desired to be sufficiently low in magnitude that conventional laboratory shock tube design and techniques could be employed. Figures 3 and 4 and Ref. 12 demonstrate that these design criteria are easily satisfied. An additional consideration for the design criteria for the shock tube system was the run time or data acquisition time available for the measurement. For incident shock wave studies, run times of 10-50  $\mu$ sec were considered to be adequate provided that a laser source of pulse width  $\tau_L \leq 1$   $\mu$ sec was used. Obviously, a variety of lasers satisfies this requirement, including the Q-switched ruby laser, the frequency-doubled Nd:YAG laser, and the excimer laser sources. Further, for reflected shock wave studies, the available data acquisition time is increased, and it was desired that reflected shock run times on the order of 500  $\mu$ sec or greater exist. If this requirement is satisfied, not only can Q-switched and other nominal 20  $\mu$ sec sources be used, but also, if the background radiation and laser-induced fluorescence or scattering are sufficiently small, it is possible to employ the more energetic conventional pulsed ruby laser of nominal 600  $\mu$ sec laser pulse width; the use of such a source will increase significantly the S/N ratio of the detected signal.

Although of lesser importance for cross section studies than the reflected shock mode of operation, consideration will be given initially to the less complex incident shock wave. For this mode of operation, the duration of the shocked gas flow time is defined to be the interval of time between the passages of the incident shock and contact surfaces. Figure 5 shows the  $x-t$  trajectory diagram for the incident shock (Ref. 12). From Fig. 5 it is noted that the incident, and assumed constant, shock speed is  $W_S$  and that the contact surface is moving with a constant speed  $V_2$ . For an arbitrary location  $X$  in the driven section, the run time  $\Delta\tau_i$  of the incident shock wave is shown in Fig. 5. It is easily shown that  $\Delta\tau_i$  is given by

$$\Delta\tau_1 = \frac{X}{V_2} - \frac{X}{W_S} \quad (8a)$$

$$= \left(\frac{X}{a_1}\right) \left\{ \frac{[(\gamma_1 - 1) M_1^2 + 2]}{[2M_1(M_1^2 - 1)]} \right\} \quad (8b)$$

Figure 6 shows the variation of the product  $\Delta\tau_1 a_1/X$  with incident Mach number  $M_1$  for  $\gamma_1 = 1.40$ . If  $N_2$  is assumed to be the driven gas and  $X$  is selected to be 3 m, one finds  $\Delta\tau_1$  to be approximately 990  $\mu\text{sec}$ .

Increasing the position of observation increases  $\Delta\tau_1$ , as Eq. (8b) shows, until one reaches the position  $X_c$ , shown in Fig. 5, where the reflected rarefaction head intersects the more slowly moving contact surface. Clearly,  $\Delta\tau_1$  is maximum at  $x = X_c$ . The coordinates  $X_c$  and  $\tau_c$  at which this intersection occurs are given by

$$X_c = \tau_c \left\{ \frac{2a_1(M_1^2 - 1)}{[(\gamma_1 + 1) M_1]} \right\} \quad (9a)$$

and

$$\tau_c = \left( \frac{2X_4}{a_4} \right) \left\{ 1 - \frac{(\gamma_4 - 1)}{(\gamma_1 + 1)} \times \left( \frac{a_1}{a_4} \right) \times \frac{(M_1^2 - 1)}{M_1^2} \right\}^{\frac{-(\gamma_4 + 1)}{2(\gamma_4 - 1)}} \quad (9b)$$

where  $X_4$  is the length of the driver section which is charged with a gas species characterized by the isentropic sound speed  $a_4$ , and it has been assumed that the flow behind the contact surface is supersonic.

At  $x = X_c$ , the maximum run time  $\Delta\tau^+$  is given by

$$\Delta\tau_1^+ = \tau_c - \tau_s \quad (10a)$$

$$= X_c \left[ \frac{1}{V_2} - \frac{1}{W_S} \right], \quad (10b)$$

where

$$W_S = M_1 a_1$$

and

$$V_2 = \frac{2 a_1(M_1^2 - 1)}{[(\gamma_1 + 1) M_1]}$$

It can be shown that

$$\Delta\tau_i^+ = \tau_c \left\{ 1 - \frac{2(M_1^2 - 1)}{(\gamma_1 + 1)M_1^2} \right\} \quad (11)$$

Assuming that the driver and driven gas temperatures are equal and that  $\gamma_4 = 5/3$  and  $\gamma_1 = 7/5$ , evaluation of Eqs. (9) - (11) for  $X_4 = 2.4$  m and  $M_1 = 4$  yields  $\Delta\tau_i^+ = 1.25$  msec, which is consistent with the desired performance of the tube.

Considering the reflected shock region, the observation time ( $\Delta\tau_r$ ) can be shown (Ref. 12) to be given by

$$\Delta\tau_r = \frac{X_2}{V_2} - \frac{X_1}{W_S} \quad (12)$$

where  $X_1$  is the driven length and  $X_2$  is the distance from the diaphragm to the position of interaction of the reflected shock and the contact surface. Further,

$$X_2 = X_1 \frac{\left[ \left( \frac{1}{W_R} \right) - \left( \frac{1}{W_S} \right) \right]}{\left[ \left( \frac{1}{W_R} \right) - \left( \frac{1}{V_2} \right) \right]} \quad (13)$$

where  $W_R$  is the speed of the reflected shock and is given by

$$\frac{W_R}{W_S} = \frac{\left\{ 2 + \left[ 2 \frac{\left( \frac{P_1}{P_2} \right)}{(\gamma_1 - 1)} \right] \right\}}{\left\{ [(\gamma_1 + 1)] - \left( \frac{P_1}{P_2} \right) \right\}} \quad (14)$$

Figure 7 shows the variation of  $\Delta\tau_r$  with the length  $X_4$  and  $X_1$  of the driver and driven sections, respectively, for an incident Mach 3 shock wave. Selecting  $X_4$  and  $X_1$  to be 2.1 m and 4.6 m, respectively, it is seen that  $\Delta\tau_r = 635$   $\mu$ sec is obtained as the observation time; this value of  $\Delta\tau_r$  corresponds to the nominal conventional model pulse width of the Holobeam Model 620 ruby laser which is to be used for the cross-section studies. Using these selected values of  $X_4$  and  $X_1$ , the variation of  $\Delta\tau_r$  with  $M_1$  was calculated, and the results are shown in Fig. 8. It is seen from Fig. 8 that, as known from the outset, the use of a nominal 20-nsec laser pulse width is adequate for reflected shock studies, but, additionally, it is seen that, subject to restrictions which were mentioned previously about background radiation and other noise sources, the more energetic conventional mode ruby laser is capable of utilization for reflected shock studies for the Mach number range  $2 \leq M_1 \leq 3$ . Consequently, from these results it is seen that the desired observation times, as well as the desired temperatures and densities, can be achieved with a shock tube of reasonable practical lengths and  $P_4/P_1$  pressure ratios.

## 2.2 NON-IDEAL EFFECTS OF SHOCK TUBE OPERATION

A variety of effects degrades the performance of a practical shock tube relative to the behavior of the ideal system. Although the quantitative evaluation of the majority of these effects must be obtained by calibration measurements of the shock tube, it is informative to list and discuss briefly some of these effects and note their relative importance.

### 2.2.1 Boundary-Layer Formation

The interaction of the shock tube wall with a real gas results in the formation of a boundary layer whose effect and importance increases with decreasing unit Reynolds number of the gas. Figure 9 sketches the boundary layer which is formed initially at the shock front and continues its growth through the region of the shocked gas. The importance of this phenomenon can be attributed to three major effects its existence has on shock tube studies: (1) reduction in shock flow and observation time; (2) modification of the conversion of laboratory to particle-time scale; and (3) nonuniform shock wave properties. Each of these effects will be considered.

First, regarding the reduction in shock flow time, it has been a common observation (Ref. 12) for shock tube studies that the observation time of shock tube experiments was significantly less than the ideal shock tube predictions. Mirels (Ref. 14) has summarized these findings and presented a quantitative explanation of the phenomenon. The trajectory diagram of Fig. 10 shows that the distance between the shock front and the contact surface increases for an ideal shock wave. However, as Mirels shows, the formation of the boundary layer results in a maximum shock length ( $\ell_m$ ) as the contact surface accelerates to conserve the mass of the "2" region gas which is processed by either the boundary layer or the contact surface regions. Upon achieving this steady-state condition, the shock wave proceeds with a constant length ( $\ell$ ) of shocked gas for which  $\ell = \ell_{max}$ . This non-ideal behavior is sketched in Fig. 10, and, using the previously-defined observation time parameter  $\Delta\tau$ , Fig. 10 shows clearly, albeit qualitatively, the reduction in  $\Delta\tau$  for a real shock tube. Equally clear, but qualitative, is the dependence of the resulting test time reduction on the degree of turbulence of the boundary condition. Mirels presented results based upon the assumptions of boundary layers which were either laminar or turbulent, but no predictions were presented for the case for a boundary layer which was characterized by the transition from laminar to turbulent. More recently, Bander and Sanzone (Ref. 15) have considered the problem and have shown that for such a transitional case  $\Delta\tau$  can be expressed as

$$\Delta\tau = \frac{\Delta\tau_i}{2} + (1/2) \left[ (\Delta\tau_i)^2 + 4 t_{fl}(\Delta\tau_i - \Delta\tau_i) \right]^{1/2} \quad (15)$$

where  $\Delta\tau_t$  and  $\Delta\tau_l$  denote the turbulent and laminar test times, respectively, and  $t_{tr}$  is the laboratory time at which transition to turbulence occurs. Note that the relation  $t_{tr} = 0$  defines a fully turbulent boundary layer and, for this case,  $\Delta\tau = \Delta\tau_t$ . For a completely laminar flow,  $t_{tr} = \Delta\tau_l = \Delta\tau$ . Obviously, the crucial parameter of Eq. (15) is  $t_{tr}$ . For the shock wave conditions studied in Ref. (15), it was found that  $t_{tr}$  was given by equating the transition Reynolds number  $(Re)_t$  and flow Reynolds number  $(Re)_s$

$$(Re)_t = (Re)_s \tag{16}$$

where  $(Re)_t$  was defined to be

$$(Re)_t = \frac{V_2^2 t_{tr} \rho_2}{\eta_2} \tag{17}$$

where  $(Re)_s$  was

$$(Re)_s = \frac{V_2 D \rho_2}{\eta_2} \tag{18}$$

The shock tube diameter is  $D$ , and the gas speed, mass density, and viscosity are denoted by  $V$ ,  $\rho$ , and  $\eta$ , respectively. From Eq. (16) and the relations of Eqs. (17) and (18), one finds the nondimensional time to transition,  $\bar{t}_{tr}$ , to be given by

$$\bar{t}_{tr} = \frac{t_{tr}}{\left(\frac{D}{a_1}\right)} = \frac{(1/2)(\gamma_1 + 1)M_1}{(M_1^2 - 1)} \tag{19}$$

which is the time required for the shocked gas to travel a length of one tube diameter. Therefore, if the results of the rather restricted study of Ref. 15 are valid, the test time of a shock tube flow is predictable.

The second major effect of the boundary layer is the required modification to the magnitude of the particle time  $t_p$ . The laboratory time  $t_l$  of a shock wave is the time duration at an observation location, as measured by conventional instrumentation, between the passage of the shock front and the time of measurement of a property of the gas sample within the observation or measurement volume, i.e.,

$$t_l = \int_0^l \frac{d\ell'}{W_S} = \frac{\ell}{W_S} \tag{20}$$

In shock-fixed coordinates the time ( $t_p$ ) required for a particle to pass from the shock front to the distance  $\ell$  downstream of the shock is

$$t_p = \int_0^{\ell} \frac{d\ell'}{u_2} \tag{21}$$

where  $u_2$  is the speed of the gas in the shock-fixed coordinate system. If uniform shock conditions exist, it is easily seen that

$$t_p = t_\ell \left( \frac{n_2}{n_1} \right) \quad (22)$$

which is significantly greater than  $t_\ell$ .

Since it is the particle time ( $t_p$ ) which is relevant for rate kinetics and nonequilibrium calculations for shock waves, it is quite clear that knowledge of  $t_p$  is essential for the design of experiments which are based upon the assumption of LTE and yet which utilize gaseous molecular species for which energy transfer relaxation processes exist. For such studies, therefore, knowledge of  $t_p$ , supplemented by appropriate rate kinetics calculations, will enable prediction of the required delay in measurement following passage of the shock front to ensure LTE for the molecular species.

Hobson and his co-workers (Refs. 16, 17, and 18) recognized the implications of Mirels' results for the calculation of  $t_p$  and showed that for a laminar boundary layer

$$\frac{t_p}{t_p^{(0)}} = -2 \left( \frac{\ell}{\ell_m} \right)^{-1} \left\{ \left( \frac{\ell}{\ell_m} \right)^{1/2} + \ln \left[ 1 - \left( \frac{\ell}{\ell_m} \right)^{1/2} \right] \right\}, \quad (23)$$

where

$$t_p^{(0)} = t_\ell \left( \frac{n_2}{n_1} \right);$$

$t_p/t_p^{(0)}$  is shown in Fig. 11 as a function of  $\ell/\ell_m$ , and it is seen that the correction is significant. The relations used for the calculation of  $\ell_m$  are given in Ref. 14 and will not be reproduced here.

In addition to the two boundary-layer effects which have been discussed previously, there exists a third effect which can introduce systematic errors in cross section measurements obtained with the shock tube. This third effect is the existence of nonuniform gas properties between the shock front and contact surface locations. It is necessary, as a result of this nonuniformity, to be able to predict values of the shocked gas properties as a function of the gas sample's axial distance  $\ell$  from the shock front. Mirels (Ref. 19) has considered this complication and has shown that for a shock Mach number  $M_s$  for a gas of specific heat ratio  $\gamma$

$$\frac{\Phi_{2\ell}}{\Phi_{2s}} = \frac{[2 + (\gamma - 1) M_{2s}^2]}{[2 + (\gamma + 1) M_s^2]} \quad (24)$$

where the subscripts "2 $\ell$ " and "2s" represent values of  $\Phi$  at  $\ell$  and at the shock front, respectively. Further,  $\Phi$  denotes  $T$ ,  $n^{\gamma-1}$ , and  $p^{(\gamma-1)/\gamma}$ . Further, as shown in Ref. 19, the Mach number of the flow directly behind the shock in shock-fixed coordinates is

$$M_{2s} = \left\{ \frac{[(\gamma - 1) M_s^2 + 2]}{[2\gamma M_s^2 - (\gamma - 1)]} \right\}^{1/2} \quad (25)$$

and the Mach number  $M_2$  at any location  $\ell/\ell_m$  is obtained by numerical solution of the equation

$$M_2 = \left[ 1 - \left( \frac{\ell}{\ell_m} \right)^{1/2} \right] M_{2s} \times \left\{ \frac{[2 - (\gamma - 1) M_2^2]}{[2 + (\gamma - 1) M_{2s}^2]} \right\} \frac{(\gamma + 1)}{[2(\gamma - 1)]} \quad (26)$$

To obtain an estimate of the maximum variation of the gas parameters within the shock, use is made of the ratio given in Ref. 19 of the properties at the contact surface ( $\Phi_{2c}$ ) and downstream of the shock front ( $\Phi_{2s}$ ). These results were tabulated by Mirels for  $\gamma = 5/3$ ,  $7/5$  and  $6/5$ , and these results are shown in Figs. 12 and 13. Figure 12 shows the temperature ratio  $T_{2c}/T_{2s}$ , and it is seen that  $T_{2c}/T_{2s}$  decreases as  $M_s$  increases. For  $\gamma = 5/3$ , it is seen that the corrections for  $M_s = 2$  and  $M_s = 50$  are 12 percent and approximately 7 percent, respectively. For  $\gamma = 7/5$ , these corrections are approximately 7 percent and 4 percent, respectively. As Eq. (24) and Fig. 13 show, even larger variations exist for the ratio  $n_{2c}/n_{2s}$ . As an example, from Fig. 13,  $n_{2c}/n_{2s}$  for  $\gamma = 7/5$  are approximately 18 percent and 8 percent for  $M_s = 2$  and 50, respectively. Although  $\Phi_2/\Phi_{2s}$  will be less than  $\Phi_{2c}/\Phi_{2s}$ , it is clear that accurate cross section measurements require consideration of the effects of nonuniform shocked gas properties, and, although not presented in this report, these results have been extended to predict the temporal variation of the shocked gas properties in the reflected shock region.

### 2.2.2 Real-Gas Effects

The equations and relations of the previous sections have assumed the shocked gas species to be ideal, since the specific heat ratio  $\gamma$  and the chemical constituency were assumed to be constant. However, as the gas temperature increases, the energy of excitation of the internal and electronic modes of motion of the molecule increases. Consequently,  $\gamma$  decreases as  $T$  increases, which introduces real-gas effects into the derivation of the shock tube relations. The qualitative result of these real-gas effects produces post-shock values of the temperature and density which are lower and higher, respectively, than the ideal gas results. Similar effects result from consideration of dissociative reactions of the shocked gas species.

The excitation and dissociative reaction processes described in the previous paragraph occur with finite characteristic times or rate kinetics coefficients, and recognition that these processes do not occur with infinite speed introduces an additional complication in prediction of the shocked gas parameters. The qualitative features of these processes are most easily appreciated by considering the vibrational relaxation mechanism for excitation of the vibrational mode of a simple diatomic species such as  $N_2$ . If the vibrational mode is assumed to be in local thermal equilibrium and to be characterized by a vibrational temperature  $T_v$  corresponding to a molar vibrational energy  $\tilde{E}_v$ , it is known that the time variation of  $\tilde{E}_v$  is given by (Ref. 20).

$$\frac{d\tilde{E}_v}{dt} = - \left( \frac{1}{\tau_v} \right) [\tilde{E}_v - \tilde{E}_{ve}], \quad (27)$$

where  $\tau_v$  is the vibrational relaxation time and  $\tilde{E}_{ve}$  is the molar vibrational energy if the mode were in equilibrium with the gas translation temperature. The vibrational temperature  $T_v$  is related to  $\tilde{E}_v$  by the relation

$$\tilde{E}_v = \frac{R\theta_v}{\left[ \exp\left(\frac{\theta_v}{T_v}\right) - 1 \right]} \quad (28)$$

where it is assumed that the diatomic molecule is characterized by a simple harmonic oscillator of characteristic vibrational temperature  $\theta_v$ .  $R$  is the universal gas constant.

As  $N_2$  is processed by the shock front, which is several mean free paths in thickness, the relaxation time  $\tau_v$  is sufficiently long and the rotational mode relaxation time  $\tau_R$  is sufficiently short that  $N_2$  behaves as a gas with an approximate  $\gamma$  of 7/5. Consequently, the temperature and density increase through the shock front follow, in the main, the path for a  $\gamma = 7/5$  gas, and this is shown for the temperature increase in Fig. 14. Following this increase in both rotational and translational temperatures through the shock, vibrational excitation becomes significant, and  $\tilde{E}_v$  attempts to relax toward the variable value of the translational temperature  $T_{tr}$  which is assumed to equal the rotational temperature  $T_R$ ; i.e.,  $T_{tr} = T_R = T$ .

Since an increase in  $\tilde{E}_v$  is supplied from the translational and rotational modes, an increase in  $\tilde{E}_v$  and, therefore,  $T_v$ , results in decreasing values of  $T_{tr}$  and  $T_R$ , as shown in Fig. 14. Quite clearly, if measurements of the Raman spectra of the vibrational modes of molecular motion are to be observed, the speed with which vibrational equilibrium is attained is a crucial parameter for cross section measurements.

Since  $\tau_v$  for most diatomic species is described by the Landau-Teller theory which predicts that  $\tau_v$  varies as  $\exp(T^{-1/3})$ ,  $\tau_v$  decreases rapidly as T increases (Ref. 20). Consequently, more rapid vibrational relaxation is expected for high Mach number shots and for the reflected shock region. However, prediction of this effect is essential for accurate shock tube studies. Although they will not be reported in this work, such calculations have been performed for  $N_2$  and binary mixtures of  $N_2$  and  $O_2$ , and  $N_2$  and  $H_2O$ , and the effect of the boundary-layer formation on this collisional phenomenon has been included in the computation. For this report, the measurements of the vibrational Raman spectra have been restricted to temporal regions in the shock flow which are either late in the incident shock or early in the reflected shock regions. Therefore, even though relaxation calculations are required for accurate predictions, it is ensured that significant vibrational excitation will exist.

### 3.0 SHOCK TUBE SYSTEM

#### 3.1 SHOCK TUBE CONFIGURATION

Based on the experimental considerations which were either discussed or implied in the previous sections, the design criteria were determined, and the operating condition ranges and shock tube dimensions were specified. The configuration chosen was a circular cross-section tube of 6.35-cm diam with a driver section length of 2.4 m. The driven section length was 4.57 m. The mismatch in diameter of the test/driven section was 0.025 mm. However, deviations from circularity of the tubes and flanges produced a circumferentially-random maximum mismatch of 0.050 mm. To satisfy the safety requirements for operation, the driven section of the tube was fabricated from 1018 seamless steel tubing of 2.75-in. (6.99 cm) OD and 0.120-in. (0.30 cm) wall thickness. The driver section was fabricated from 2.5-in. (6.35) ID black steel pipe with a 0.250-in. (0.64 cm) wall thickness, which has a design and statically tested maximum charge pressure of 1,000 psia (68 atm). The shock tube was mounted on a 12-in. (30.5 cm) channel iron bar which, in turn, was attached to five 4-in.-(10.2 cm) diam posts. The posts were braced and bolted to the concrete floor. The design of the mounting system was such that deflection of the shock tube base during a shot would be less than or equal to 0.130 mm, and alignment was accomplished using a He-Ne laser and level. Figure 15 is a sketch of the shock tube and the mounting installation.

Before initial operation of the shock tube, it was evident that the interior wall of the tube had rusted. Operation of the shock tube in conjunction with the laser scattering system, which is described in a following section, showed that the particulate content of the shocked gas was excessively large for Raman scattering studies. To eliminate the rust problem and to minimize particulate scrubbing from the wall, annular liners of 304 stainless steel were

inserted into both the driver and driven sections of the shock tube. The liner was of 0.188-in. (0.476 cm) thickness and was press-fit into the tube, and soldering was used at the tube penetrations to achieve both vacuum integrity and stationary positioning of the liner. The final inner diameter of the tube was 2.125 in. (5.60 cm).

Diaphragm rupture is achieved by the conventional pressure burst method and, alternatively, to achieve greater shock reproducibility, if necessary, by the use of a plunger device. The plunger is located upstream of the diaphragm and is oriented at an angle of 37 deg with respect to the tube centerline. Actuation of the sharp-tipped plunger is accomplished by air pressure, and 12 msec are required to achieve the 3.8-cm extension of the plunger from its retracted position to the point where it pierces the diaphragm. The diaphragm materials used are Mylar<sup>®</sup> or annealed aluminum, depending on the shock strength desired. For modest shock strengths,  $M_1 = 4$ , one or more pieces of 1-5 mil (0.03 -13mm)-thick Mylar<sup>®</sup> are used. Larger Mach numbers and pressure ratios require the use of scribed metal diaphragms. With this plunger system, the driver section can be filled to a pressure inferior to the burst pressure, the driver gas can be stabilized, and the diaphragm plunger can be activated.

The gas charging system is divided into two parts for filling the test gas and driver gas sections. Provision has been made to cold trap the condensible impurities of the test gas. The high-pressure side is charged with He for shock operations. Because the low-pressure system needs protection from high pressure, interlocks have been included to inhibit pressure release which would be hazardous to either personnel or equipment. Firing is also inhibited until all essential valves have been closed. All firing and high-pressure charging is done remotely from a control panel on which are located the power switches for vacuum pumps, thermocouple readouts, and vacuum gauges. Nitrogen is available to purge the system and maintain a positive pressure in the tube during periods of infrequent use.

The shock tube is equipped with mechanical pumps and an oil diffusion pump for fast removal of post-shock gases, and, using these pumps, a pressure of approximately  $10^{-5}$  torr is obtainable in both the driver and driven sections. The diffusion pump cold trap is cooled to  $-30^{\circ}\text{C}$  by a ½-ton refrigerator to minimize oil backstreaming, and, as a result, the rate of outgassing is approximately 2 mTorr/min. Consequently, if the test gas pressure is 10 torr and 10 min are required to charge the gas systems and initiate the shock, the impurity level can approach 2 parts per thousand.

Relief valves in both the driver and driven sections are essential design features for protection of the shock tube and operator. In the high-pressure section, a relief valve, adjusted for 1,050 psia (71.4 atm), does not allow the design charge pressure to be exceeded.

The low-pressure section relief valve is preset at approximately 350 psia (23.8 atm) for protection of the quartz windows in the test cell.

Stack venting from both relief valves, as well as all normal high-pressure venting, is to the outdoors through 1-in.-(2.54 cm)-diam stainless steel tubing. The venting system capacity is sufficient to withstand a complete high-pressure regulator failure. Since toxic gases are not to be used initially and the pumped volume is small, the vacuum pumps have been vented to the ambient atmosphere. Modification can be simply made if stack venting is required.

### 3.2 CONVENTIONAL INSTRUMENTATION

The equations of the theoretical section show clearly that knowledge of the shocked gas parameters requires measurement of  $P_1$ ,  $P_4$ ,  $T_1$ ,  $T_4$ , and the incident shock speed  $W_S$ . Further, for operation of the tube in either the simple reflected or the tailored mode, measurements of  $P_5$  and  $T_5$  are desired. The measurements of  $P_1$  and  $P_4$  are performed using calibrated Tabor gauges which have 0.1-percent accuracy. For the  $P_4$  measurement a 2,000-psia (136 atm) gauge is used, and, at present, a 5-psia (0.34 atm) gauge is used in the driven section. Additional gauges in both sections are used to provide a visual display of the pressure. The pressure gauges, as well as the other conventional instrumentation used, are listed in Table 1.

A Kistler gauge was located in the flange at the end of the driven tube. Calibrations were performed to obtain full-scale readout at 300 psia (20.4 atm) dynamic pressure. Expected accuracy is of the order of 5 percent of full scale with a rise time of approximately 10  $\mu$ sec.

To obtain the incident shock velocity, a series of platinum heat transfer (HT) gauges were installed upstream of the test section. Figure 16 illustrates the design. The HT gauges are spaced uniformly 30.5 cm apart with the last gauge 1 m from the end of the tube. Engelhard 05-X platinum paint was brushed across a 6.35-mm-diam quartz substrate and fired to produce a strip of platinum approximately 0.5-mm wide. Resistances desired and obtained for all the strips were  $50 \pm 5\Omega$ . The strips are oriented perpendicular to the shock flow for maximum time resolution. The shock velocity is obtained by measuring the time of transit of the shock front between the HT gauges, which are separated by known distances. For a Mach 4 shock, the incident shock velocity is approximately 1.4 mm/ $\mu$ sec. The time interval between successive HT gauges, assuming constant velocity, is then about 427 $\mu$ sec. The uncertainty in the time interval due to the width of the strips is about 0.7 $\mu$ sec, or approximately 0.2 percent.

### 3.3 LASER SYSTEM AND OBSERVATION CELL

Since the Raman cross section measurements are to be performed in both the incident and reflected modes, a Raman scattering observation cell has been attached, as shown in Fig. 17, to the end of the driven section of the shock tube. The cross section of the interior of the scattering cell is, of course, circular, and the tolerance of 0.050 mm was maintained for non-coincidence of the circular cross sections of the scattering cell and the driven tube section. The aluminum scattering cell includes four optical ports into each of which are positioned 3.49-cm-diam quartz windows of 6.35-mm thickness.

As shown in Fig. 17, the laser beam is injected vertically downward into the observation volume, and the incident beam is collected and dissipated by a beam collector/dump assembly which is located opposite the injection optics port. The basic laser source is a Model 620 Holobeam pulsed ruby laser which provides an output at 694.3 nm with a nominal pulse width and energy of 650  $\mu$ sec and 36 J, respectively, in the conventional mode of operation. Using a Pockels cell Q-switch, the capability exists for operation with a pulse width of 25 nsec and a pulse energy of 3 J. A single-stage amplifier is available for addition to the oscillator to increase the laser beam energy to a maximum value of approximately 6 J. Because of the observation of particulates in the shocked gas which results in laser-heated particulate incandescence, as described and demonstrated in Ref. 10, the use of frequency-doubling of the laser beam shifts the Raman scattering signal to the blue-region tail of the near-blackbody particulate incandescence spectrum. Consequently, the signal-to-incandescence noise is increased by approximately two orders of magnitude. To accomplish this wavelength shift, a rubidium dihydrogen arsenate (RDA) frequency-doubling crystal was used, and the ruby laser beam at 694.3 nm was converted with approximately 20 percent efficiency to a wavelength of 347.15 nm.

For the initial measurements, the laser oscillator was operated at an approximate output power of 500 MW and the frequency-doubled output power was approximately 100 MW. The 0.635-cm-diam beam at 347.15 nm was focused onto the centerline of the shock tube using a lens system of an effective focal length of 7.62 cm. The approximately cylindrical focal volume dimensions were 1-mm-diam and 6-mm length which yields an approximate power areal density at the scattering volume of  $10^{10}$  W/cm<sup>2</sup>. The collected scattered radiation was focused onto the 400- $\mu$ m-wide entrance slit of an 0.85- $\mu$ m focal length, double spectrometer which was found to have a typical reciprocal dispersion of 0.44 nm/mm. The dispersed radiation was passed through an exit slit of 400  $\mu$ m onto an RCA 31034

photomultiplier tube (PMT) which was operated at 2,000 V. Data acquisition and registration were achieved using a gated integrator and CRT display and photographic recording. Available for data acquisition and preliminary data reduction of the pressure gauges, the PMT, laser beam energy monitor, and heat transfer gauges was an on-line PDP-8E minicomputer system. More complete details of the laser scattering system are to be found in Refs. 1-3, 6, and 7.

## 4.0 RESULTS AND CONCLUSIONS

### 4.1 RESULTS

A series of measurements was performed to demonstrate the operation of the shock tube, its associated instrumentation, and the laser Raman scattering system for temperature measurements. For this purpose, He was used as the driver gas and  $N_2$ , a diatomic species with a well-known Raman scattering profile, was selected as the driven gas. The gas shock speed  $W_S$  was determined using heat-transfer gauges, and the variation of  $W_S$  with the diaphragm pressure ratio  $P_4/P_1$  was determined. Vibrational Raman scattering of  $N_2$  was observed at two spectral locations of the Stokes vibration-rotation band, and the vibrational temperature  $T_V$  was determined using a spectral bandpass such that the  $T_V$  measurements were comparatively insensitive to the value of the rotational temperature  $T_R$ .

The initial studies were performed with the seamless steel shock tube using both Mylar<sup>®</sup> and scribed aluminum diaphragms. The Raman scattering data using the frequency-doubled ruby laser exhibited an intolerable level of background radiation because of particulate Mie scattering and laser-induced particulate incandescence. Although a fraction of this background radiation could be attributed to particulate dust created at diaphragm rupture, it was obvious that the overwhelming majority of the signal resulted from the rust particles which were scrubbed from the interior tube wall by the shock front. The most expeditious solution to this problem was the insertion of a stainless steel tube liner into both the driver and driven sections of the shock tube; the results reported in this work were obtained using this tube liner which successfully reduced the background particulate component to approximately 10 percent of the Raman signal.

Demonstration of shock tube operation was achieved over the incident shock Mach number range of approximately 4 to 5, and the shock speed  $W_S$  was measured using arrival times of the incident shock front at the known positions of the heat-transfer gauges which were described in a previous section. For operational purposes,  $W_S$  was determined as a function of the diaphragm pressure ratio  $P_4/P_1$ , which is a primary independent experimental variable. Figure 18 shows partial results of the variation of  $P_4/P_1$  with  $W_S$ , and

it is seen that deviations from the theoretical prediction of approximately 2 to 3 percent in  $W_S$  result from a selected value of  $P_4/P_1$ . However, these differences in  $W_S$  between the theoretical and experimental are repeatable to within approximately 1 percent which determines the repeatability of a specified condition.

For the shock speed measurement, erratic performance was encountered for one of the heat-transfer gauges and for the end-wall pressure gauge, and data were acquired without their use. The result of the absence of the heat-transfer gauge was slightly worsened accuracy in the measurement of the shock speed  $W_S$ . Figure 19 shows sample data of the time history of the locus of the incident shock front. For a single measurement of  $T_v$  of  $N_2$  using Raman scattering, a series of four shots were performed: two on-band Raman data shots at wavelengths  $\lambda_0$  and  $\lambda_1$  and two off-band background shots at wavelength  $\lambda_B$ . For a single series of such shock tube firings, from the data of Fig. 19 and the data of the two additional shots it was found that

$$\begin{aligned} W_S &= (1.684 \pm 0.022) \times 10^3 \text{ m/s} \\ &= (1.704 \pm 0.008) \times 10^3 \text{ m/s} \\ &= (1.714 \pm 0.008) \times 10^3 \text{ m/s} \\ &= (1.710 \pm 0.004) \times 10^3 \text{ m/s} \end{aligned}$$

where the square root of the variance of  $W_S$  for each shot is quoted as the error in  $W_S$ . The mean value of  $W_S$  for this data set of four shots is  $\bar{W}_S = (1.706 \pm 0.014) \times 10^3$  m/sec. Consequently, for a single shot, the heat-transfer gauge data yields a shock speed imprecision of less than approximately 1 percent, and the speed of a series ( $\bar{W}_S$ ) can be obtained with an imprecision level of about 1 percent. Consequently, the temperature ratio  $T_2/T_1$ , which is computed from  $W_S$  and  $M_1$ , can be expected to vary for a series of such shots by approximately 1.5 - 2.0 percent for an ideal gas case where  $\gamma$  is constant, and  $T_2/T_1$  for a single shot will be uncertain by approximately 0.5 to 1.0 percent. For this series of measurements, the mean value,  $\bar{M}_1$ , of the incident Mach number is  $\bar{M}_1 = 4.96 \pm 0.004$ . The incident shock temperature  $T_2$  is approximately 1600 K.

The malfunction of the end-wall pressure gauge had serious implications for proper timing of the laser pulse. If the laser scattering observation volume is located sufficiently far from the shock tube end-wall, timing of the laser firing and determination of the location of the laser measurement within the incident shock wave is straightforward. Measurement of  $W_S$  and the time of laser firing with respect to passage of the shock front past any one of the HT gauges will be sufficient for an accurate location of the measurement in the shock. However, if the end-wall is not located at a large distance from the observation volume and measurements are being made in the later regions of the incident shock, it is essential to

know when the incident shock reaches the end-wall. Then, assuming an ideal gas, the reflected shock speed  $W_R$ , which is obtained from (Ref. 12):

$$\frac{W_R}{W_S} = \frac{\left\{ 2 + \left[ \frac{2}{(\gamma - 1)} \right] \left( \frac{P_1}{P_2} \right) \right\}}{\left\{ \frac{\gamma + 1}{(\gamma - 1)} \frac{P_2}{P_1} \right\}}$$

is used to find the time of arrival of the reflected shock at the observation point. For  $N_2$ , for which  $\gamma$  varies from 1.4 in the incident shock to less than 1.3 in the reflected shock, one finds, for  $P_2/P_1 = 30$ , that  $V (W_R/W_S)$  equals 0.363 and 0.291 for  $\gamma = 1.4$  and 1.3, respectively. The timing of the laser firing was such that the later region of the incident shock was observed if the reflected shock were behaving as a  $\gamma = 1.3$  molecule. However, the 20-percent difference in  $W_R/W_S$  is sufficiently large that, if the vibrationally relaxing  $N_2$  is behaving at the time of the laser firing as a  $\gamma = 1.4$  species, the early region of the reflected shock was viewed rather than the end of the incident shock. This uncertainty would have been removed with accurate end-wall timing, measurements of  $P_5$ , and observation at the test volume of time of passage of the reflected shock front.

Vibrational Raman scattering measurements were performed using a calibrated single PMT channel in conjunction with the apparatus described in a previous section. To determine the wavelength or spectral locations of these measurements, Raman spectral profiles were calculated over a range of temperatures, and Fig. 20 shows the results of this calculation for the selected temperature of 2250 K for a 0.85-m focal length double spectrometer which was operated with 0.4-mm entrance and exit slit widths, a 1200 groove/mm grating and with a reciprocal linear dispersion of 0.44 nm/mm. For the range of temperatures anticipated, measurements were performed at the wavelengths of  $\lambda_0 = 377.66$  nm and  $\lambda_1 = 377.26$  nm, corresponding approximately to the peaks of Raman scattering from the  $v = 0$  and  $v = 1$   $N_2$  vibrational energy levels, respectively. The scattering signal levels at  $\lambda_0$  and  $\lambda_1$ ,  $S(\lambda_0)$ , and  $S(\lambda_1)$ , respectively, are shown in Fig. 21 as a function of the temperature, and, for the results shown in both Figs. 20 and 21, it was assumed that the  $N_2$  gas sample exhibited local thermal equilibrium; i.e.,  $T = T_v$  was assumed. Evident in Fig. 21 is the depletion in number density population of the  $v = 0$  level and the increase in population of the  $v = 1$  level as the temperature increases. Figure 22 shows the ratio  $R_v = S(\lambda_1)/S(\lambda_0)$  as a function of temperature, and the approximately linear dependence of  $R_v$  on  $T_v$  is to be noted.

Raman scattering data were acquired at the wavelength calibrated spectral locations of  $\lambda_0$  and  $\lambda_1$ . Successive shock tube firings were required for these measurements, and a series of shots was performed to obtain data at  $\lambda_0$ ,  $\lambda_1$ , and the background radiation location  $\lambda_B = 378.3$ nm where only background and particulate radiation components existed. These background data indicated signals of approximately 10 percent of the magnitude of the

Raman signals, and simple subtraction was used to correct the Raman signals for this background continuum which was assumed to vary little over the spectral band pass of the Raman measurements. Figure 23 shows typical oscilloscope traces for the Raman signals at  $\lambda_0$  and  $\lambda_1$ , and the nominal 20 nsec width and signal levels exceeding 20 mv are to be noted. For a series of measurements corresponding to  $\bar{M}_1 = 4.96 \pm 0.04$ , the values of  $T_v$  were determined and the results were  $\bar{T}_v = 2110 \pm 220$  K, where the uncertainty value of 220 K represents the standard deviation of the sample.

The measured value of  $\bar{T}_v$  exceeds the gas temperature  $T_2 = 1600$  K which was determined by  $W_S$  measurements, and the approximate 20 percent difference exceeds the estimated uncertainty in both  $\bar{T}_v$  and  $T_2$ , the latter of which is on the order of 2 to 3 percent. The most likely cause of the discrepancy between  $\bar{T}_v$  and  $T_2$  is that measurements of  $\bar{T}_v$  were performed early in the reflected shock region where  $T_v$  is increasing to its final value, which is significantly larger than both 1600 K and 2110 K. Finally, the approximately 10 percent error in  $\bar{T}_v$  is reasonably consistent with the overall uncertainty of about 7.5 percent for  $S(\lambda_0)$  and  $S(\lambda_1)$ .

## 4.2 CONCLUSIONS

The demonstration of the laser Raman-shock tube system has been accomplished, and the ability to perform Raman measurements in a shock tube environment has been shown. The necessity for operation with a stainless steel interior wall, rather than seamless steel, was shown conclusively, as was the comparatively low levels of particulate-related scattering signals with the stainless steel surface. The vibrational temperature  $T_v$  was found to be  $2110 \pm 220$  K for a series of measurements. These results were acquired using a single PMT channel for detection, and successive laser-shock tube shots were required to obtain the two signals required for the  $\bar{T}_v$  determining ratio. One or more background shots were necessary to correct for the background radiation effects. The uncertainty in  $\bar{T}_v$  could be lessened by performing at least two of these measurements during a single firing of the laser and shock tube. It is believed that uncertainty levels of  $\pm 5$  percent are obtainable in this manner.

The incident shock speed was determined using heat-transfer gauges, and it was found that the shock speed  $W_S$  could be measured with an imprecision of less than approximately 1 percent and that shot-to-shot repeatability, as reflected by  $W_S$  data, was on the order of 1 to 2 percent. Improvements in diaphragm rupture techniques could lessen this uncertainty. The shock Mach number  $M_1$  was found to be  $4.96 \pm 0.04$  for the series of  $T_v$  measurements and this value of  $M_1$  corresponds to an ideal gas temperature of approximately 1600 K. The necessity for accurate diagnostics of the reflected shock pressure and speed was made clear during the course of this study. Failure to obtain such data resulted in an uncertainty in the location within the shock of the laser scattering data. The discrepancy between  $T_2 = 1600$  K

and  $T_v = 2110$  K is suggested to arise from the acquisition of laser data to have occurred in the higher temperature reflected shock region rather than the incident shock region.

Use of the laser-shock tube system for accurate cross section and calibration measurements will require making the relatively minor and previously-mentioned experimental improvements in the system and incorporating into the theoretical analysis procedure the computational technique which predicts the effect of the relaxation processes and the boundary layer on the gas properties. These improvements are in progress at this time.

### REFERENCES

1. Williams, W. D., Wagner, D. A., Powell, H. M., and Price, L. L. "Laser-Raman Flow-Field Diagnostics of Two Large Hypersonic Test Facilities." AEDC-TR-79-88 (AD-A078289), December 1979.
2. Lewis, J. W. L., and Williams, W. D. "Profile of an Anisentropic Nitrogen Nozzle Expansion." *The Physics of Fluids*, Vol. 19, No. 7, July 1976, pp. 951-959.
3. Lewis, J. W. L., Williams, W. D., Price, L. L., and Powell, H. M. "Nitrogen Condensation in a Sonic Orifice Expansion Flow." AEDC-TR-74-36 (AD-783254), July 1974.
4. Williams, W. D., Sinclair, D. W., and Price, L. L. "Laser-Raman/Rayleigh Diagnostics Techniques Applied to Subsonic Flow." AEDC-TR-80-20 (AD-A091695), October 1980.
5. Hillard, M. E. and Emory, M. L. "An Experimental Study in the Application of the Raman Scattering Technique as a Remote Sensor of Gas Temperature and Number Density in Hypersonic  $CF_4$  Flow." AIAA Paper No. 72-1018, September 1972.
6. Williams, W. D., McCay, T. D., Powell, H. M., and Lewis, J. W. L. "Experimental Study of the Plume Characteristics of a New Monopropellant Hydrazine Thruster." AEDC-TR-79-54 (AD-A080556), January 1980.
7. Williams, W. D., Powell, H. M., Price, L. L., and Smith, G. D. "Laser-Raman Measurements in a Ducted Two-Stream, Subsonic  $H_2$ /Air Combustion Flow." AEDC-TR-79-74 (AD-A078112), December 1979.
8. Smith, J. R. "Pulsed Raman Measurements in a Stratified Charge Engine" *AIAA Journal*, Vol. 18, No. 1, January 1980, pp. 118-120.

9. Stenhouse, I. A., Williams, D. R., Cole, J. B., and Swords, M. D. "CARS Measurements in An Internal Combustion Engine." *Applied Optics*, Vol. 18, No. 22, 15 November 1979, pp. 3819-3825.
10. Williams, W. D., Lewis, J. W. L., and Jones, J. H. "Measurements of Temperature and Nitrogen Number Density in the Combustion Cylinder of a CI Engine Utilizing Laser-Raman Diagnostics." AEDC-TR-80-55 (AD-A094221), September 1980.
11. Gaydon, A. G. *Spectroscopy of Flames*. Wiley, New York, 1957, pp. 79, 90, 241.
12. Gaydon, A. G. and Hurlle, I. R. *The Shock Tube in High-Temperature Chemical Physics*. Reinhold Publishing Corporation, New York, 1963.
13. Lapp, M., Goldman, L. M., and Penney, C. M. "Raman Scattering from Flames." *Science*, Vol. 175, 10 March 1972, pp. 1112-1115.
14. Mirels, H. "Test Time in Low-Pressure Shock Tubes." *The Physics of Fluids*. Vol. 6, No. 9, September 1963, pp. 1201-1214.
15. Bander, J. A. and Sanzone, G. "Shock Tube Chemistry. 1. The Laminar-to-Turbulent Boundary Layer Transition." *Journal of Physical Chemistry*, Vol. 81, No. 1, January 1977, pp. 1-3.
16. McLaren, T. I. and Hobson, R. M. "A Study of Ionization Phenomena in a Shock Heated Gas." Report ST/66/101, Queen's University of Belfast, Belfast, Northern Ireland, September 1966.
17. Fox, J. N. and Hobson, R. M. "An Investigation of Electron Loss Mechanisms in Shock Heated Gas Flows." Report ST/66/104, Queen's University of Belfast, Belfast, Northern Ireland, October 1966.
18. Fox, J. N., McLaren, T. I., and Hobson, R. M. "Test Time and Particle Paths in Low-Pressure Shock Tubes." *The Physics of Fluids*, Vol. 9, No. 12, December 1966, pp. 2345-2350.

19. Mirels, H. "Flow Nonuniformity in Shock Tubes Operating at Maximum Test Time." *The Physics of Fluids*, Vol. 9, No. 10, October 1966, pp. 1907-1912.
20. Cottrell, T. L. and McCoubrey, J. C. *Molecular Energy Transfer in Gases*. Butterworths, London, 1961.

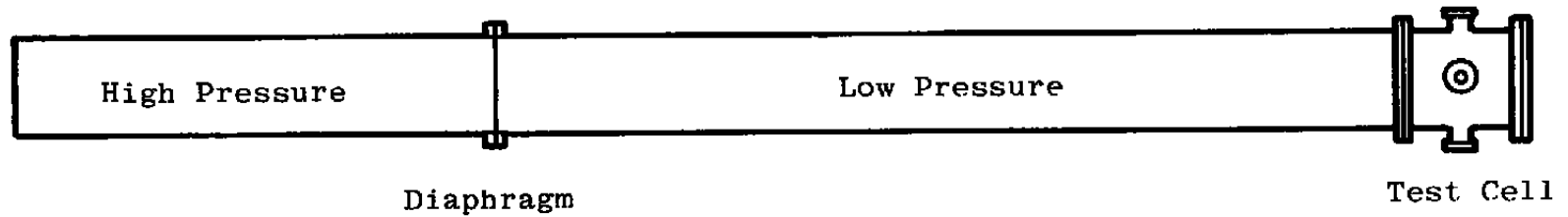


**Figure 1. Typical shock tube configuration for reflected mode operation.**

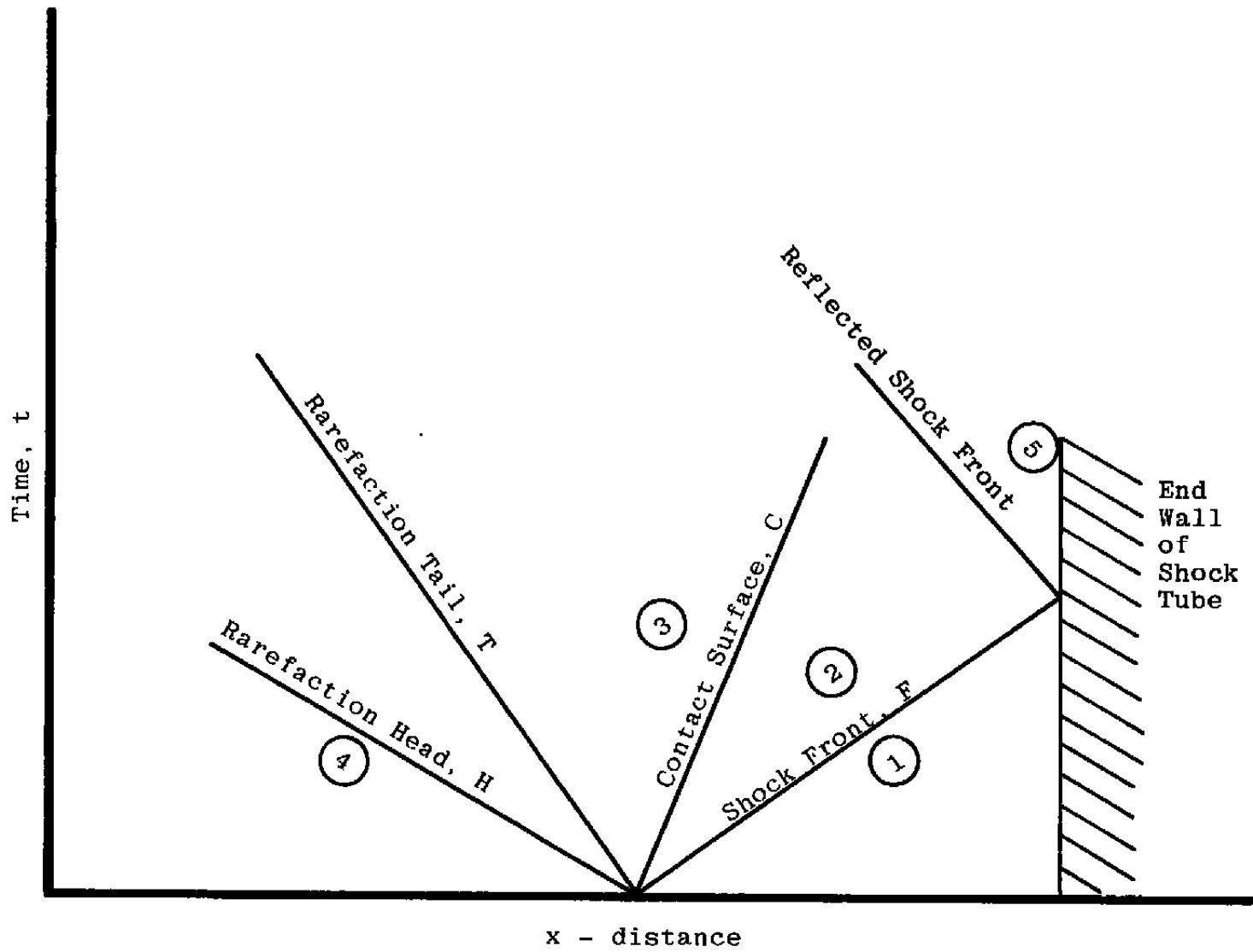


Figure 2. Diagram of shock tube regions at time  $t$  after diaphragm rupture.

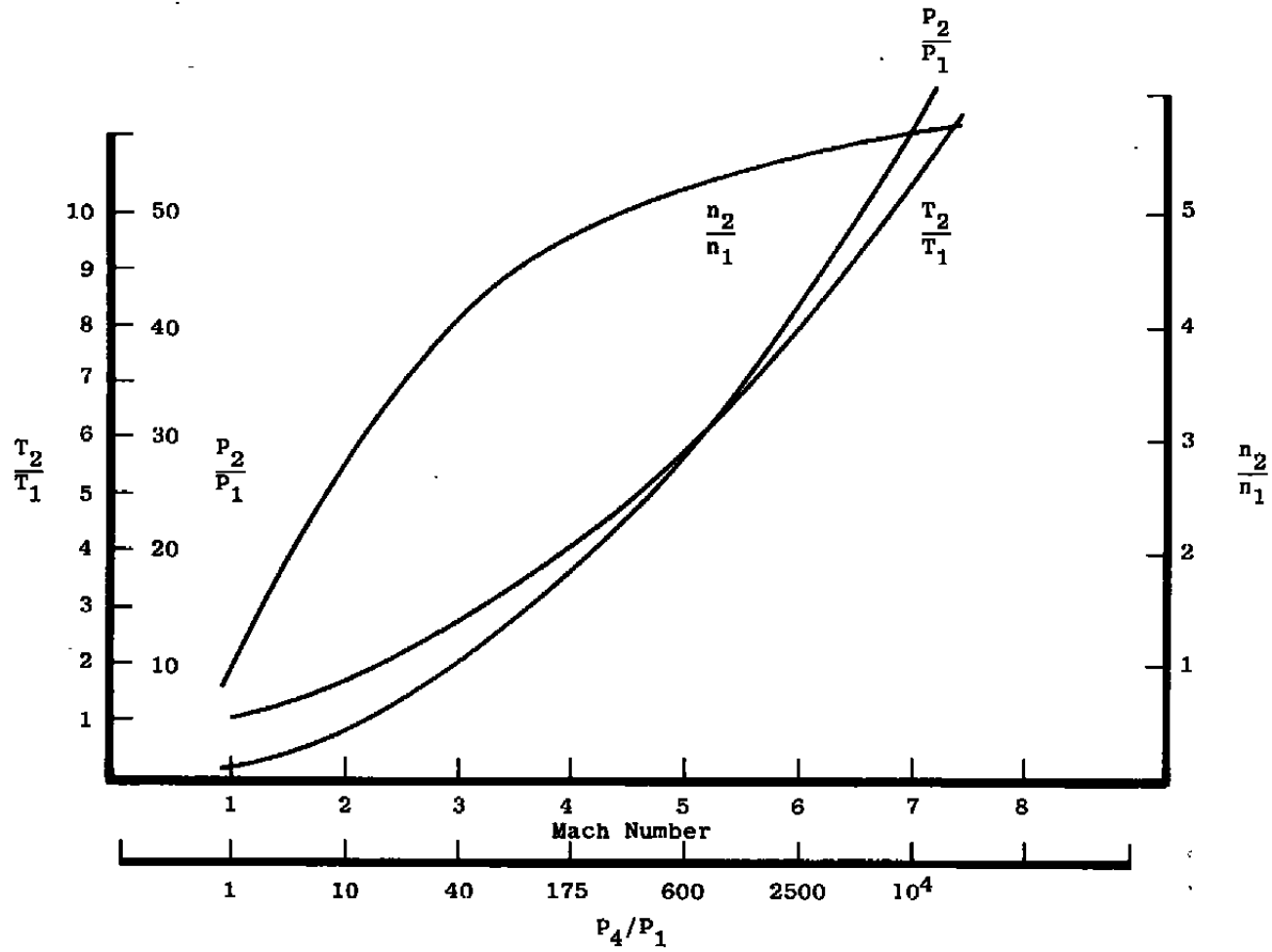


Figure 3. Ideal gas temperature, pressure, and number density ratios for nitrogen shocks.

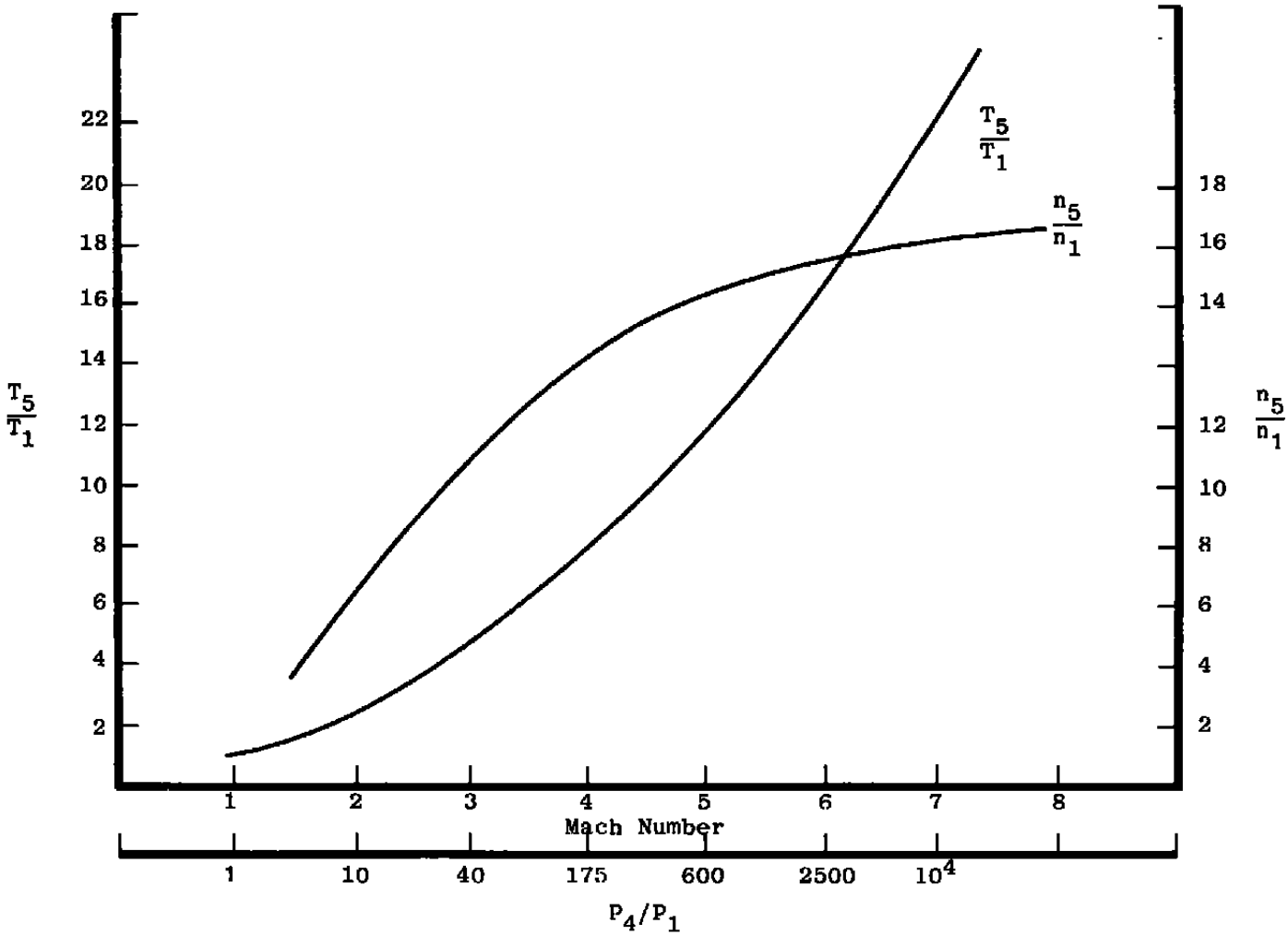


Figure 4. Ideal gas temperature and number density ratios for nitrogen reflected shocks.

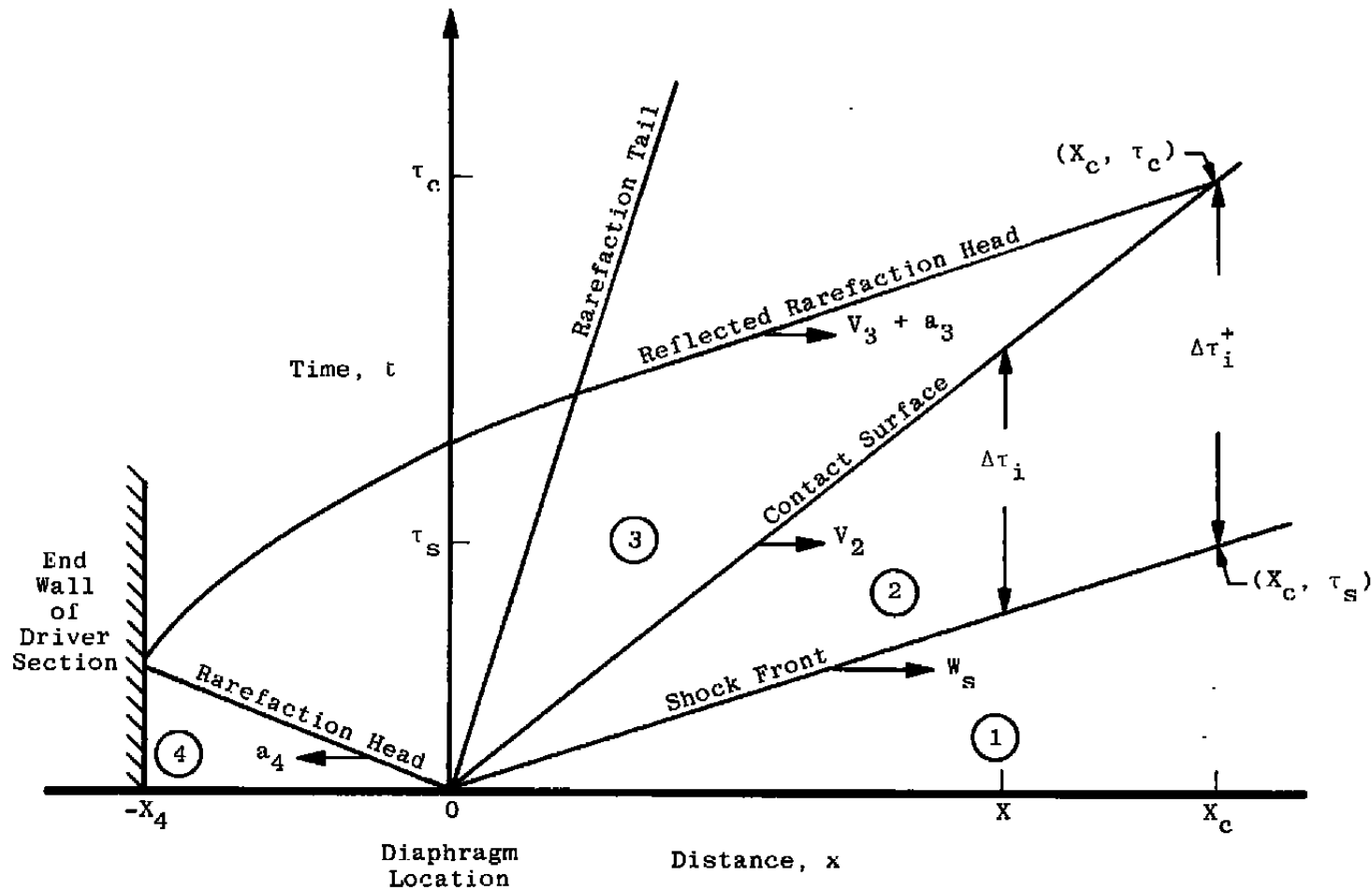


Figure 5. Shock tube time - position loci diagram.

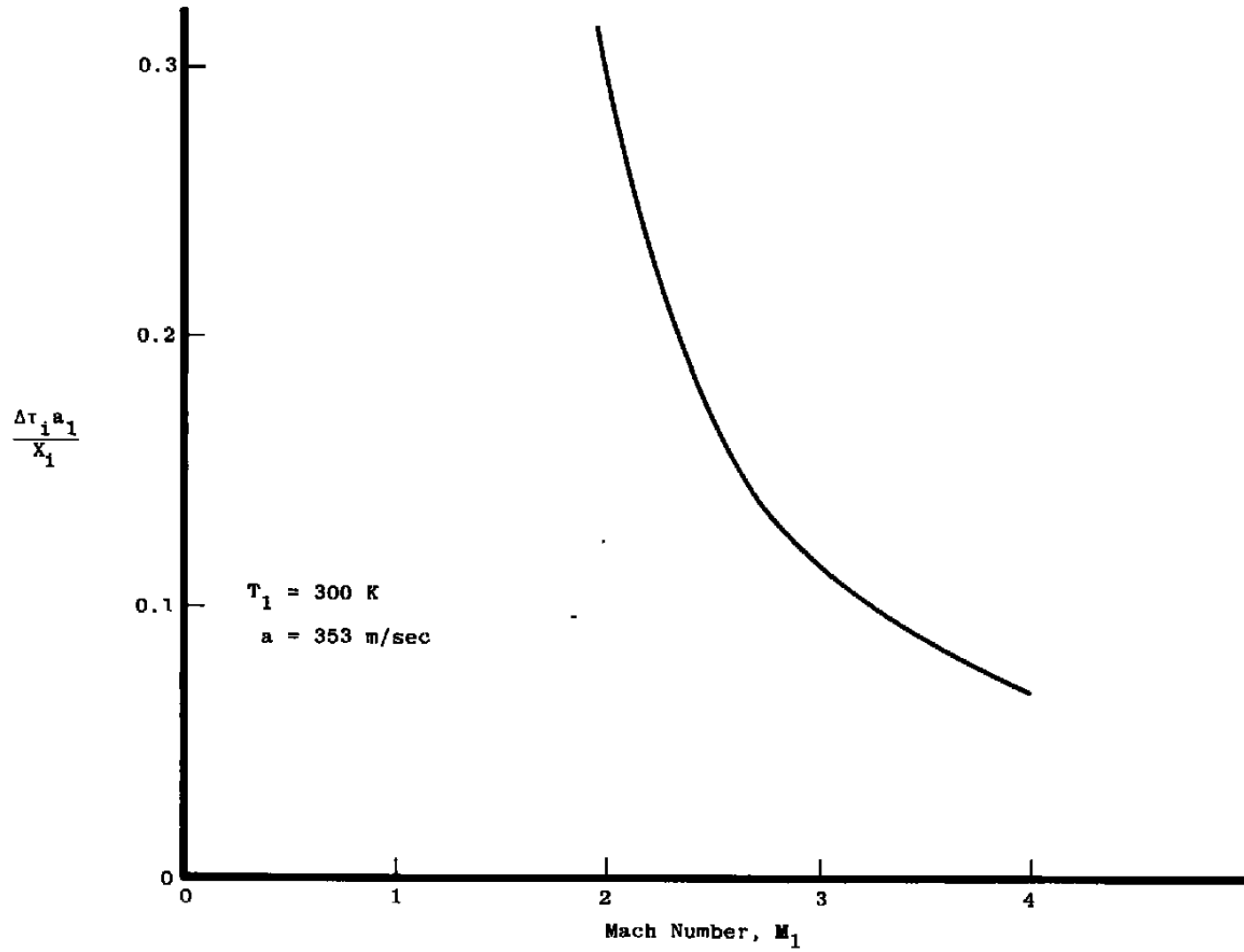


Figure 6. Incident shock flow time for  $N_2$  versus Mach number  $M_1$ .

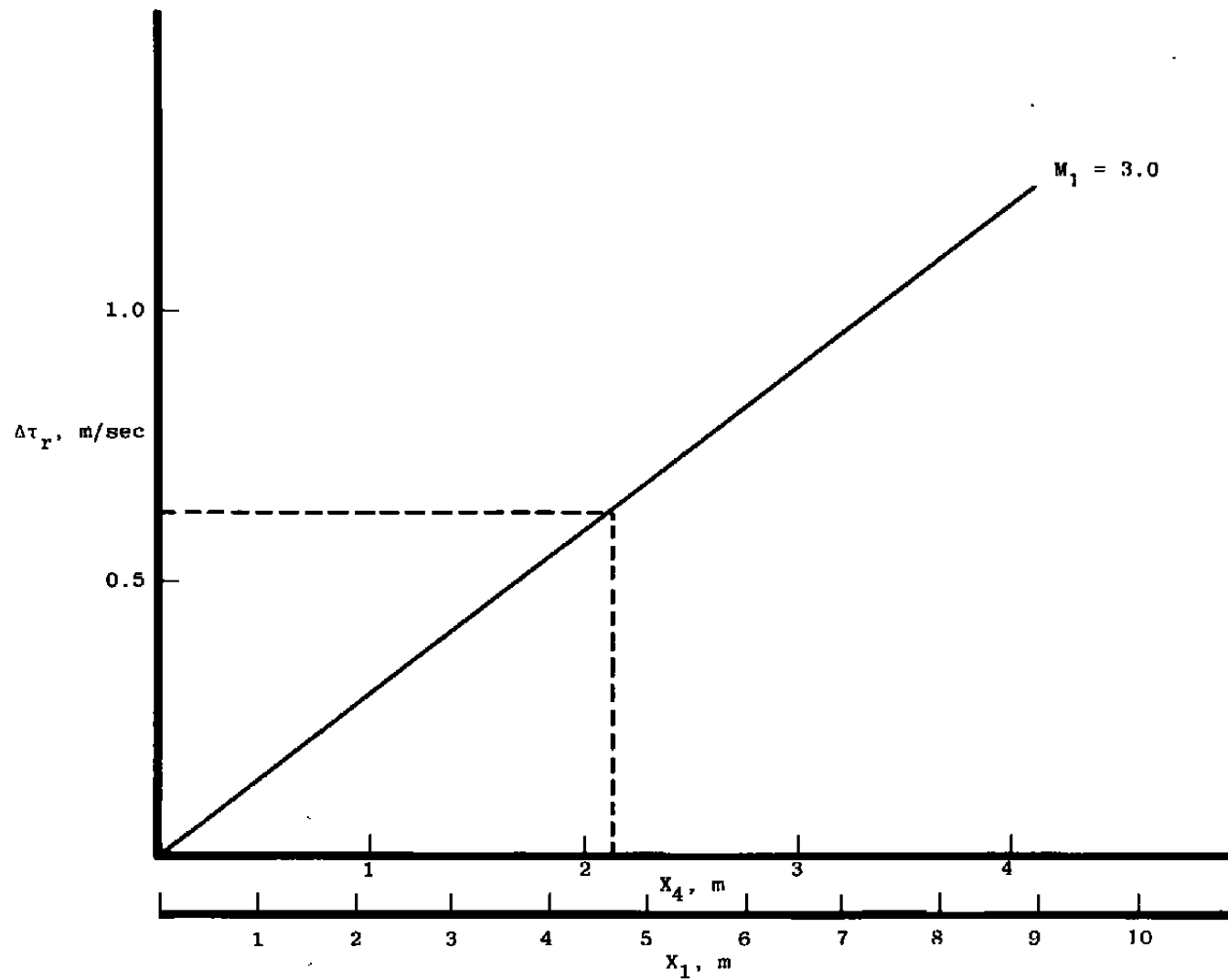


Figure 7. Reflected flow time versus driver and driven tube lengths at Mach 3.

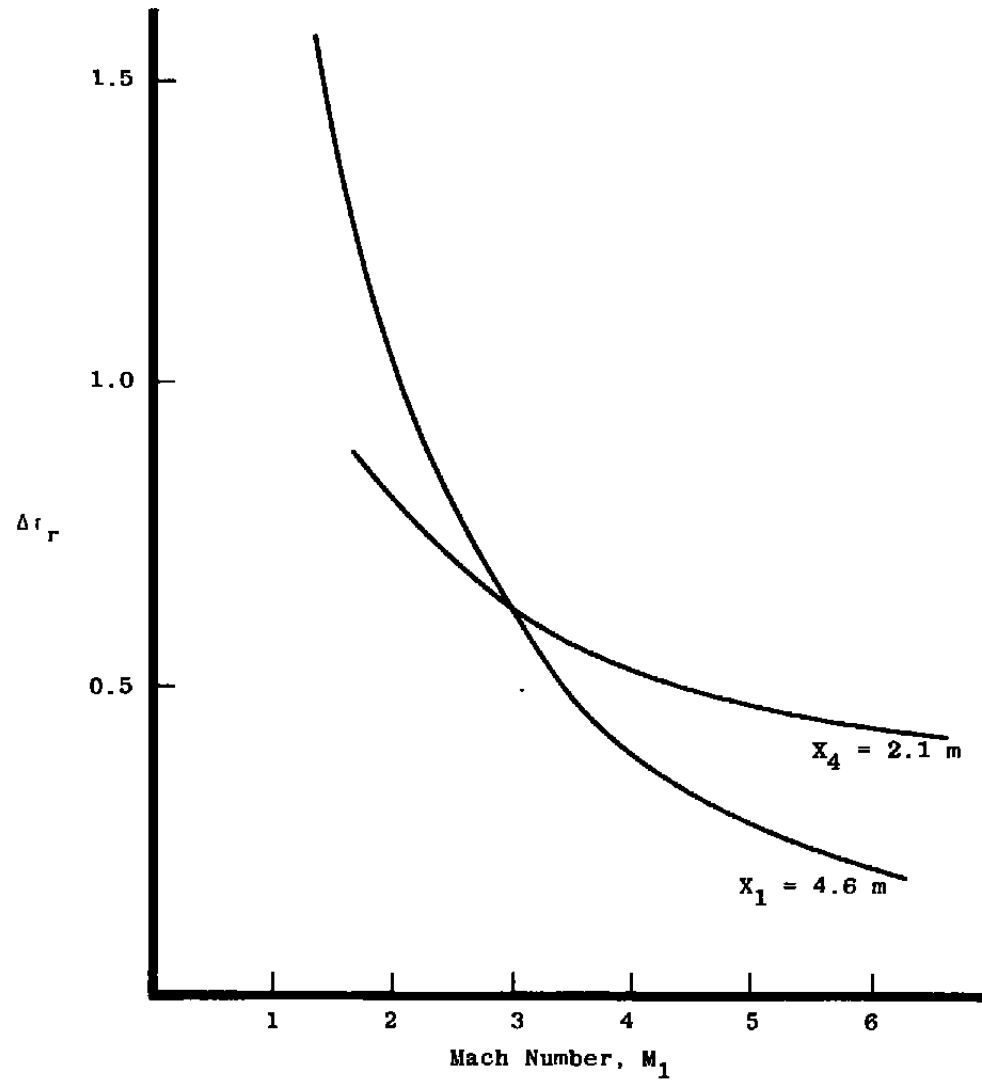


Figure 8. Reflected flow time versus Mach number for driver and driven lengths.

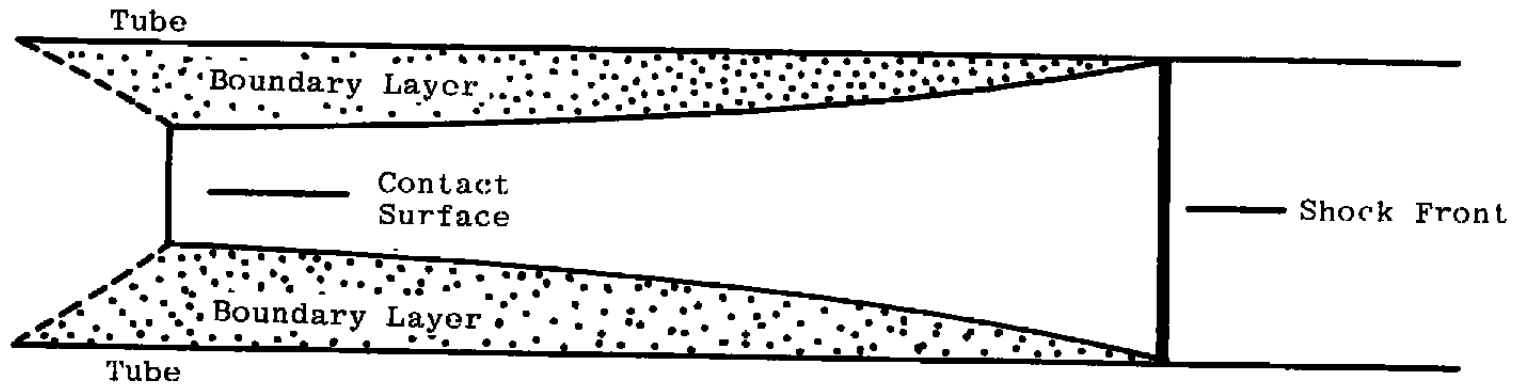


Figure 9. Boundary layer in shocked gas.

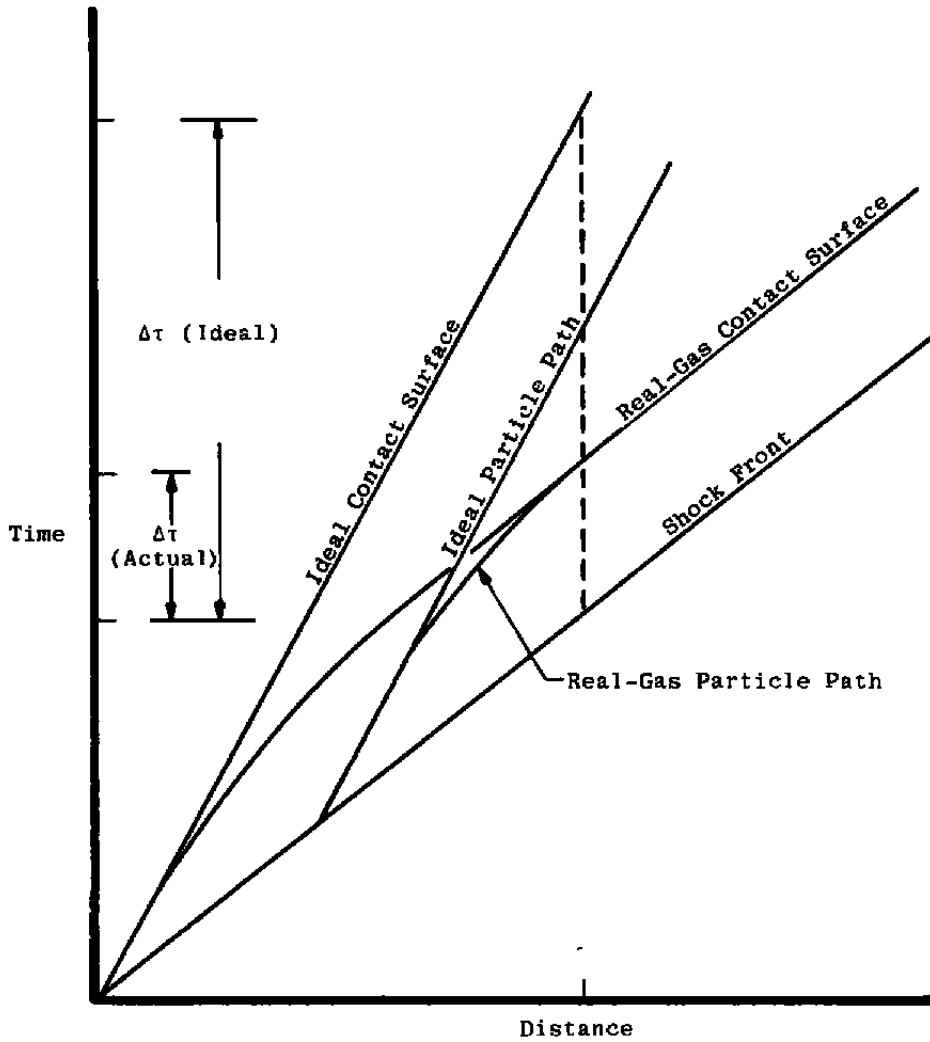


Figure 10. Trajectory diagram.

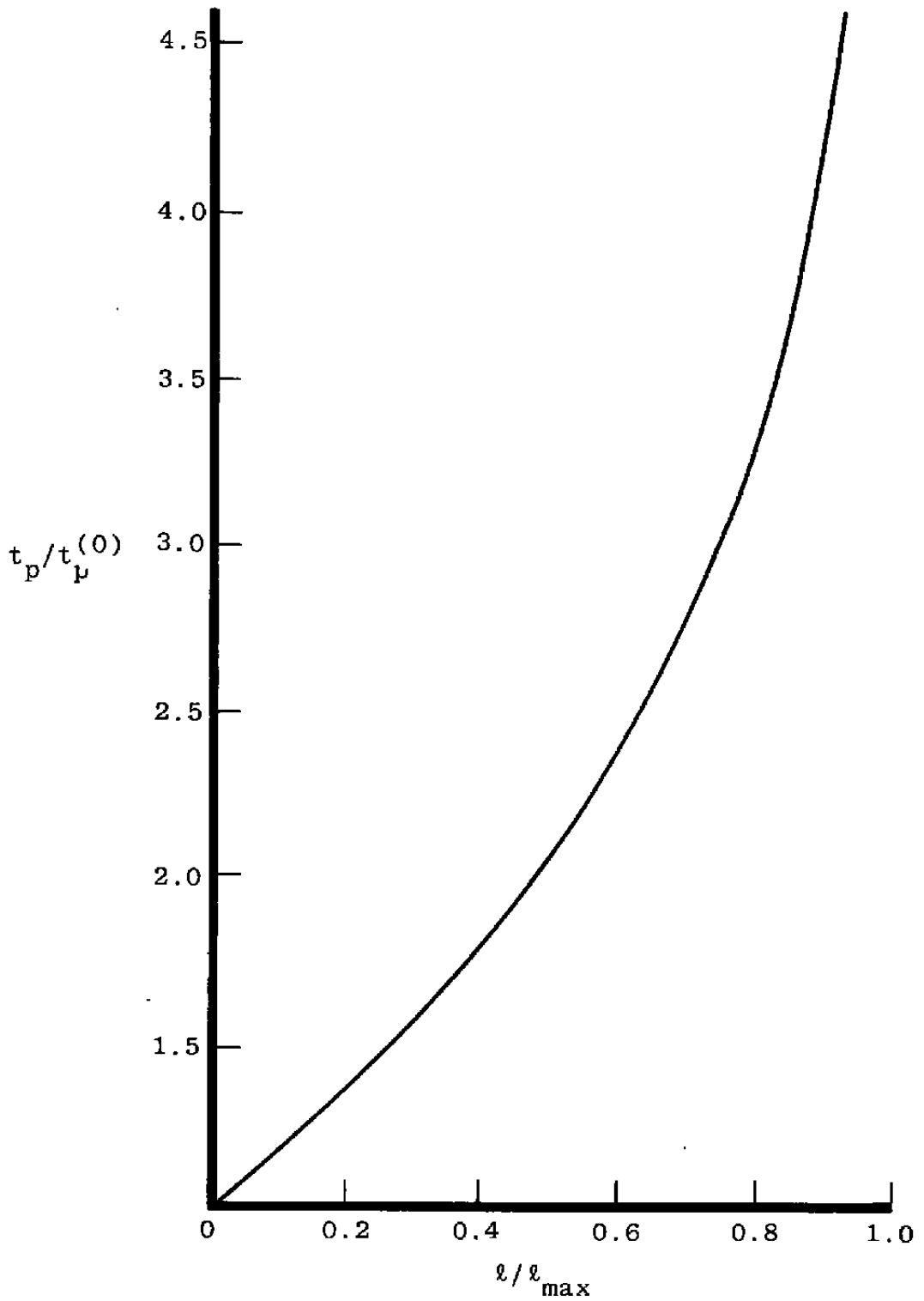


Figure 11. Particle time as a function of shock distance.

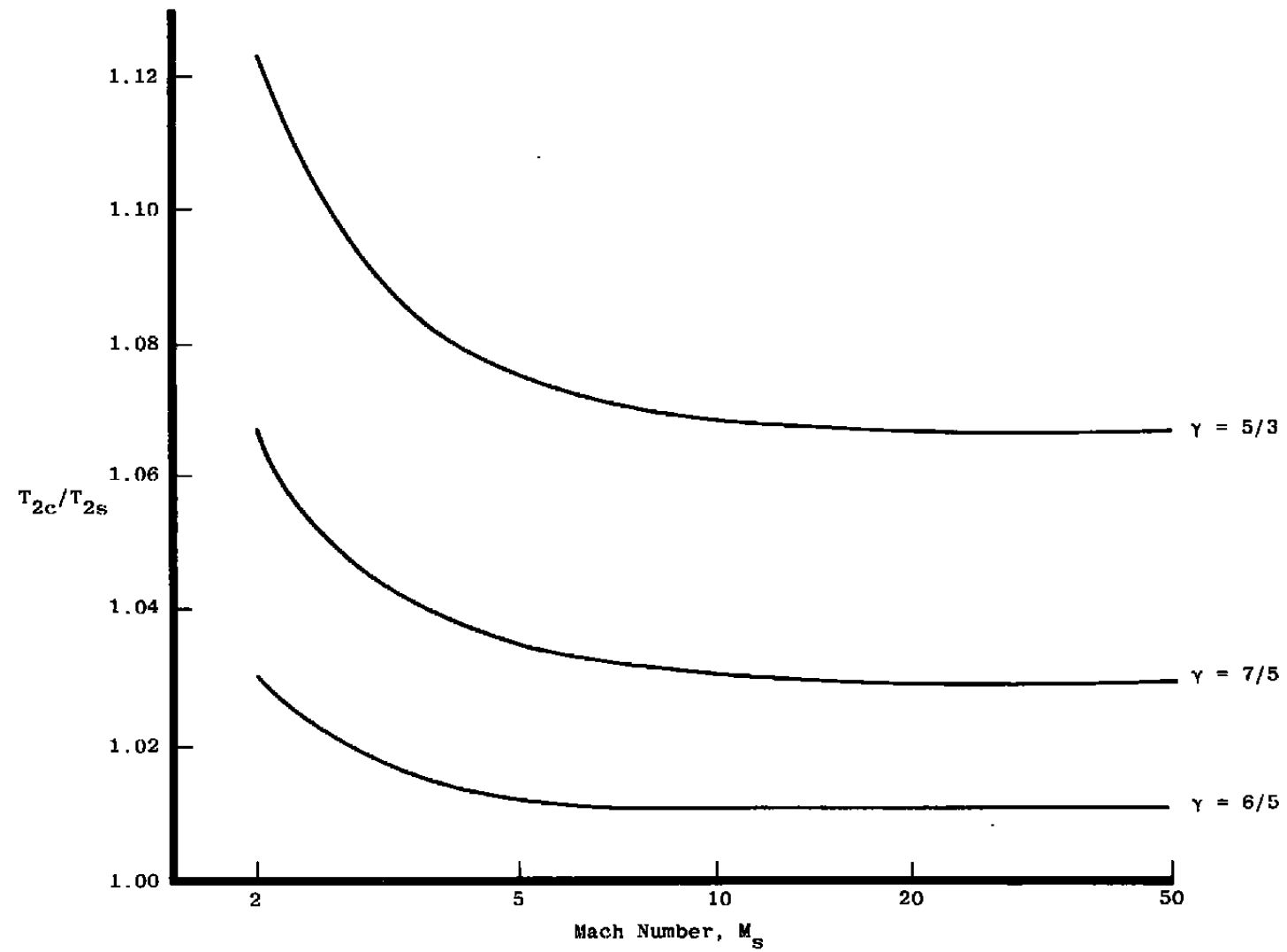


Figure 12. Variation of temperature ratio  $T_{2c}/T_{2s}$  with Mach number  $M_s$ .

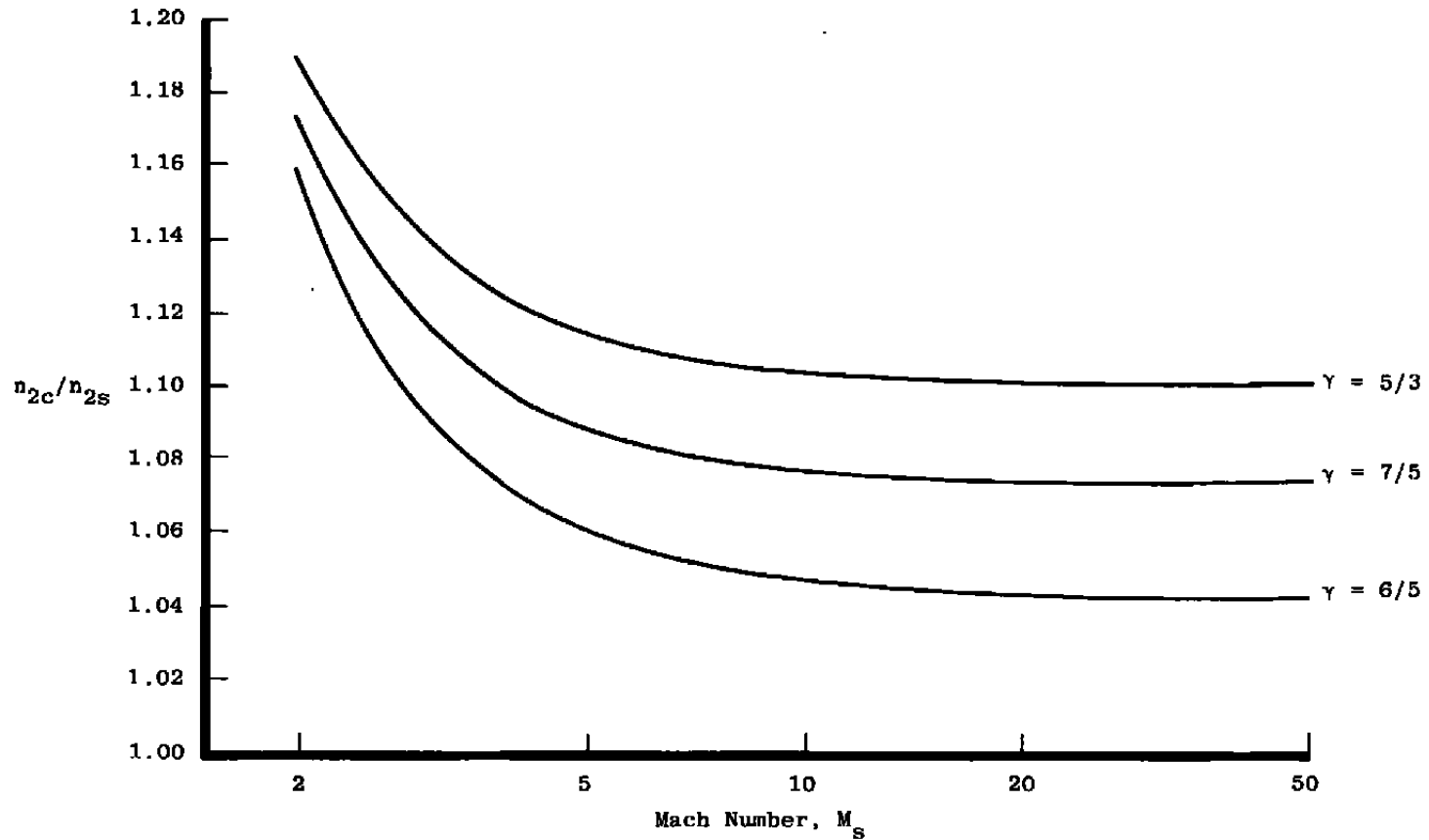


Figure 13. Variation of number density ratio  $n_{2c}/n_{2s}$  with Mach number  $M_s$ .

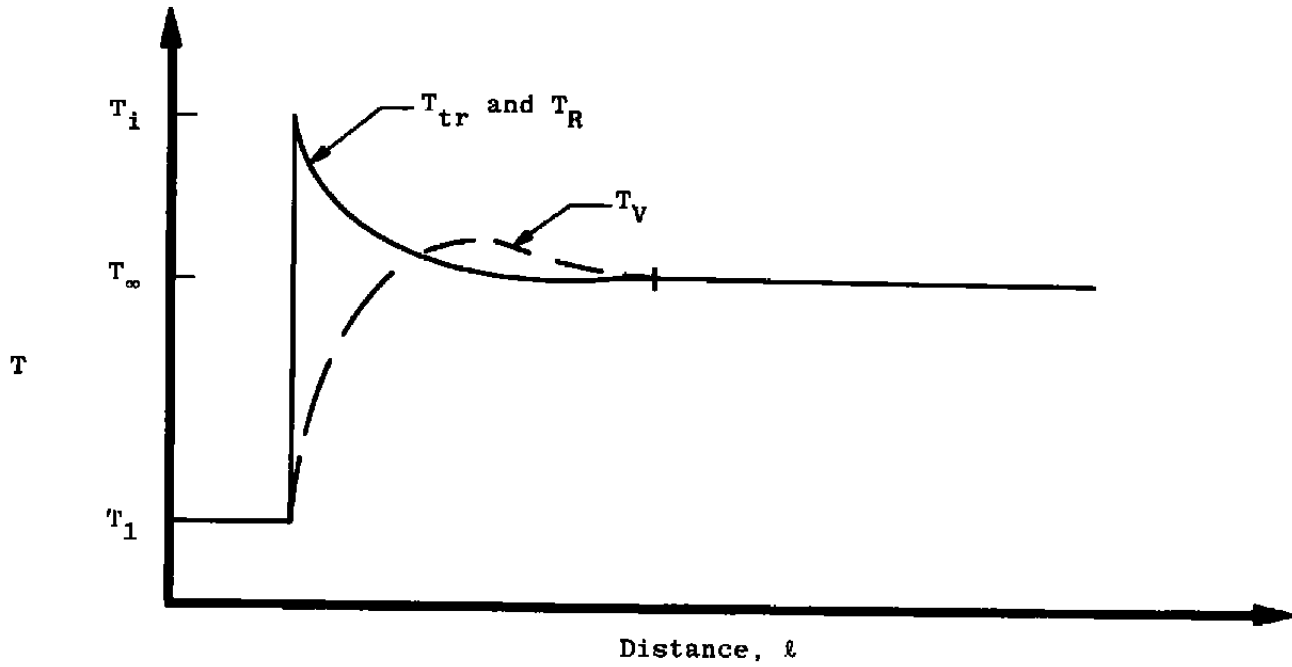
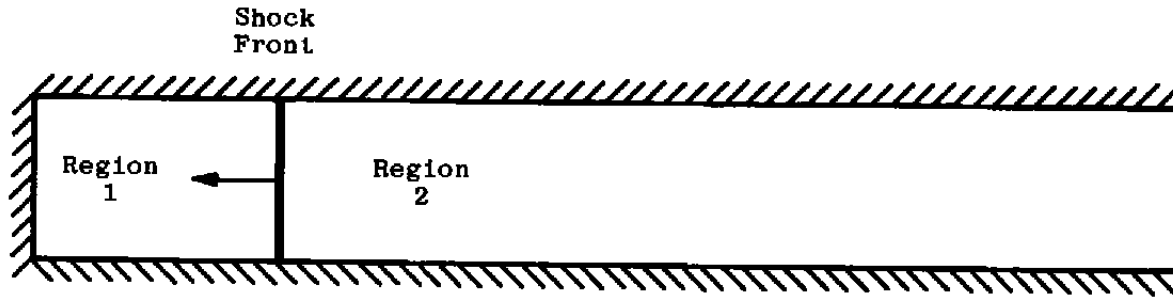
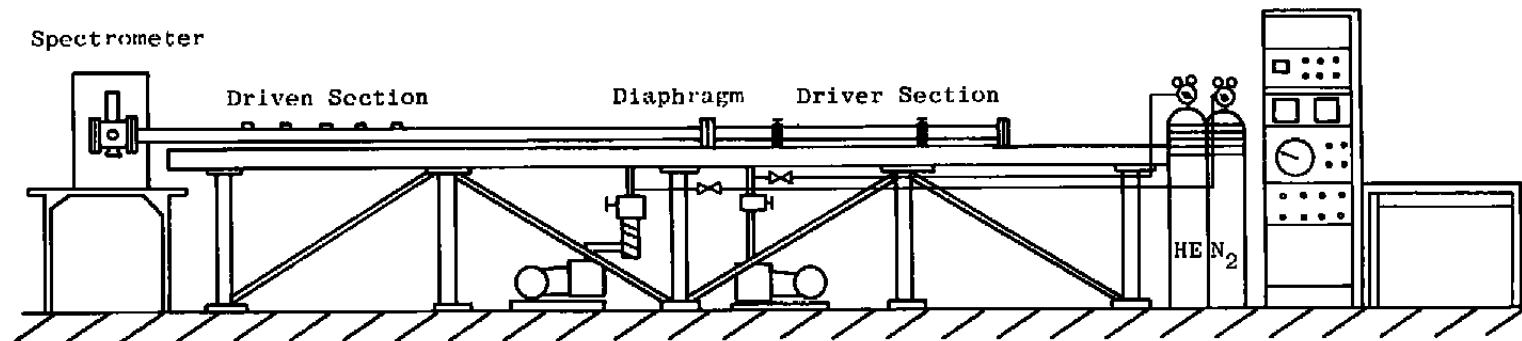
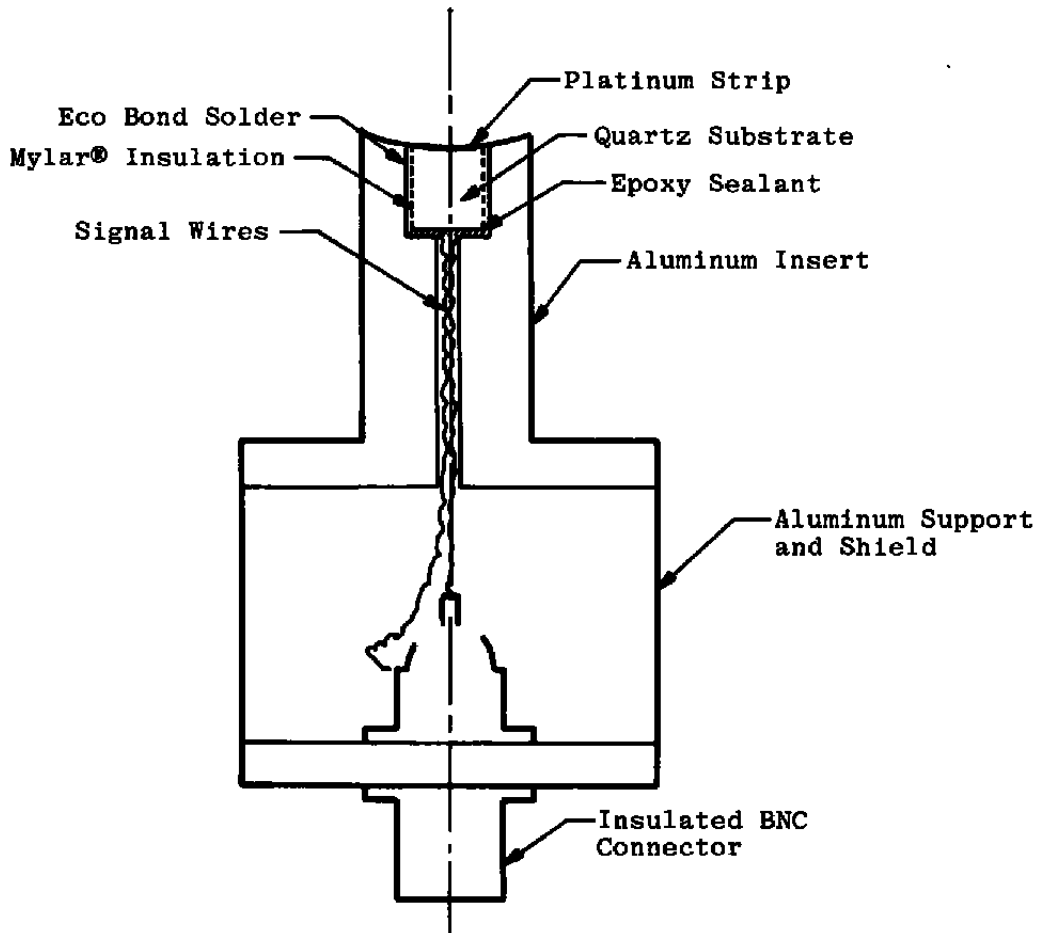


Figure 14. Sketch of variation of shocked gas temperatures with distance  $l$  into region 2.



**Figure 15. Shock tube and mounting installation.**



**Figure 16. Platinum heat-transfer gauge insert.**

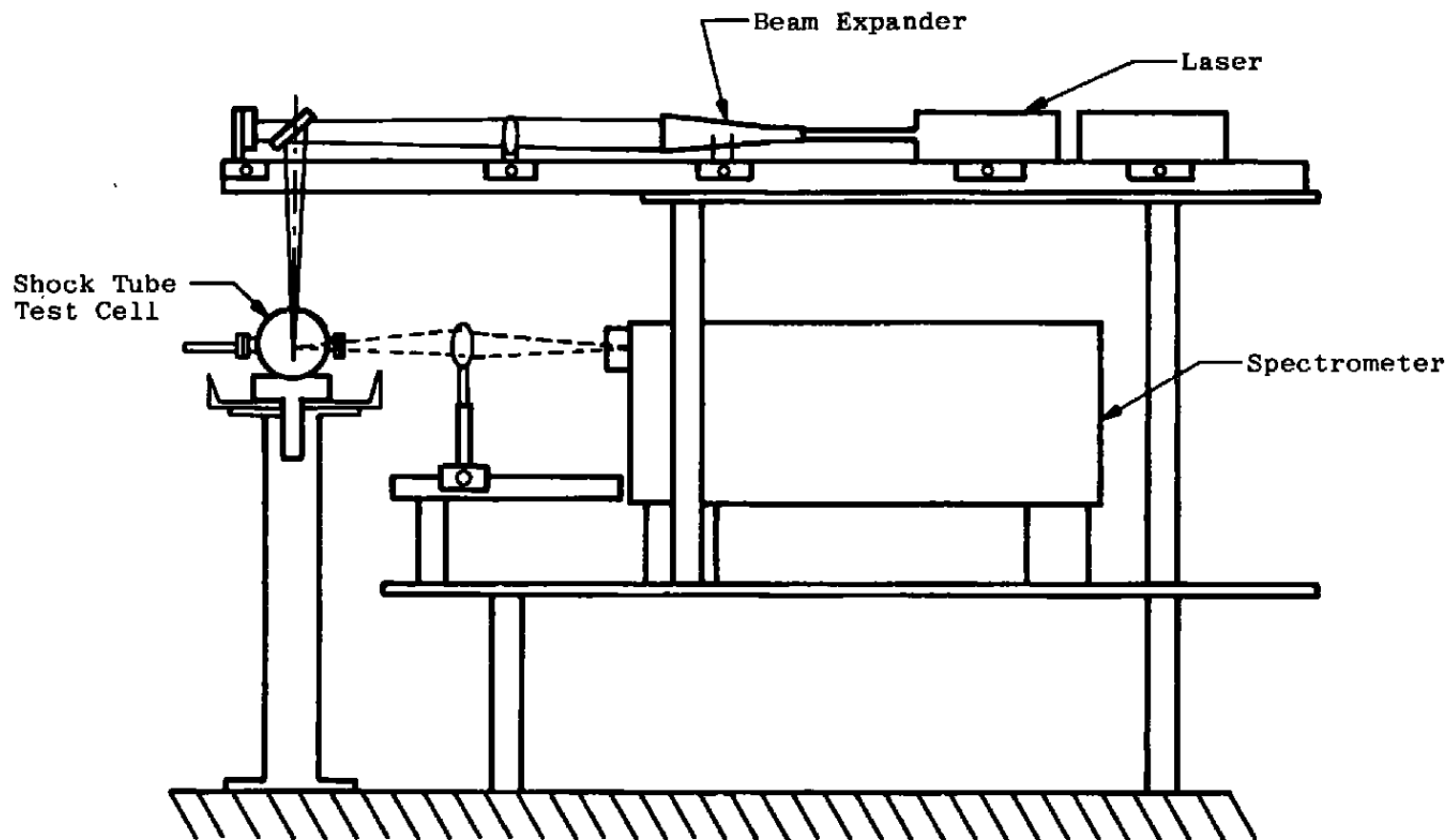


Figure 17. Shock tube test cell, laser, and spectrometer configuration.

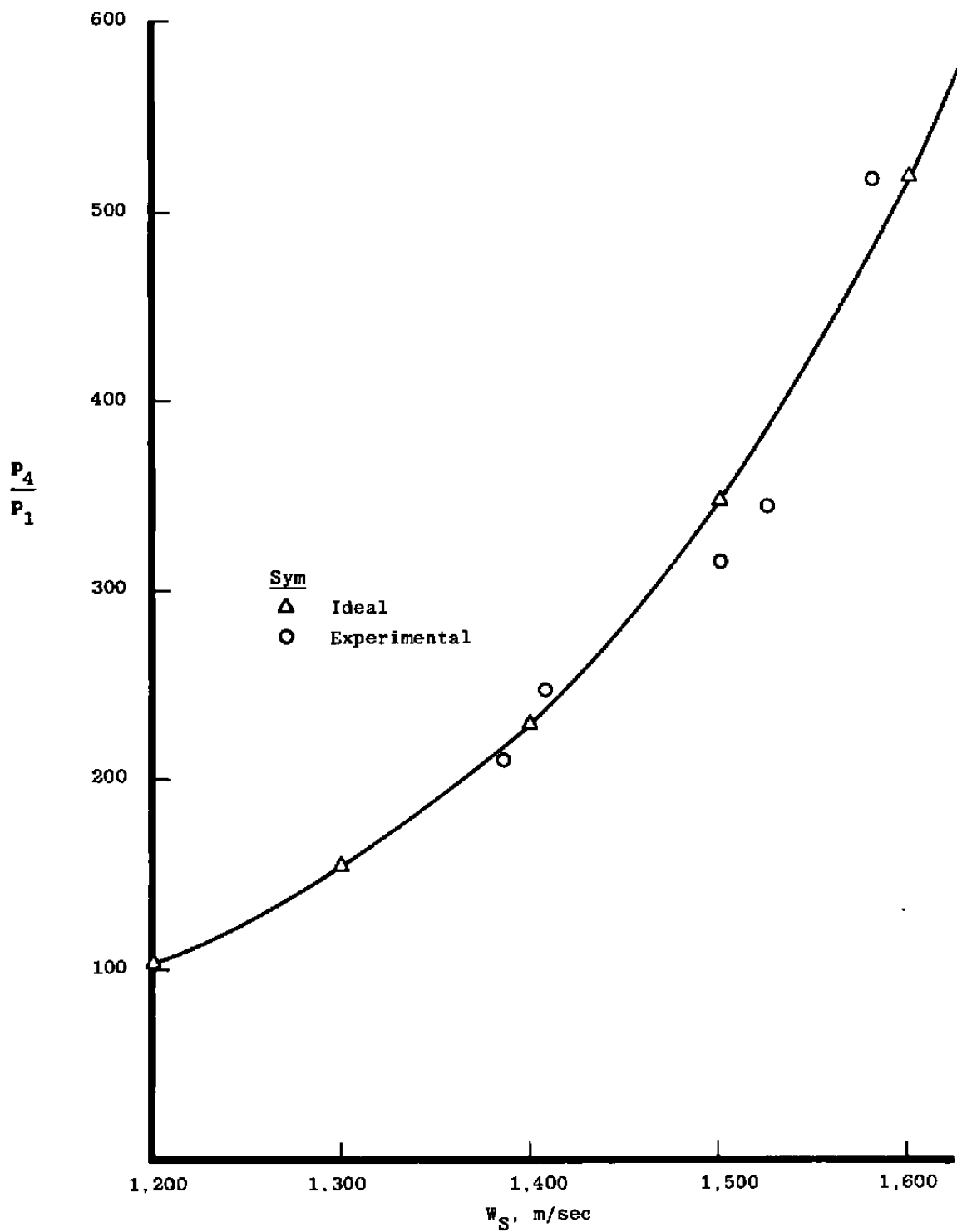


Figure 18. Pressure ratio  $P_4/P_1$  versus shock speed  $W_s$ .

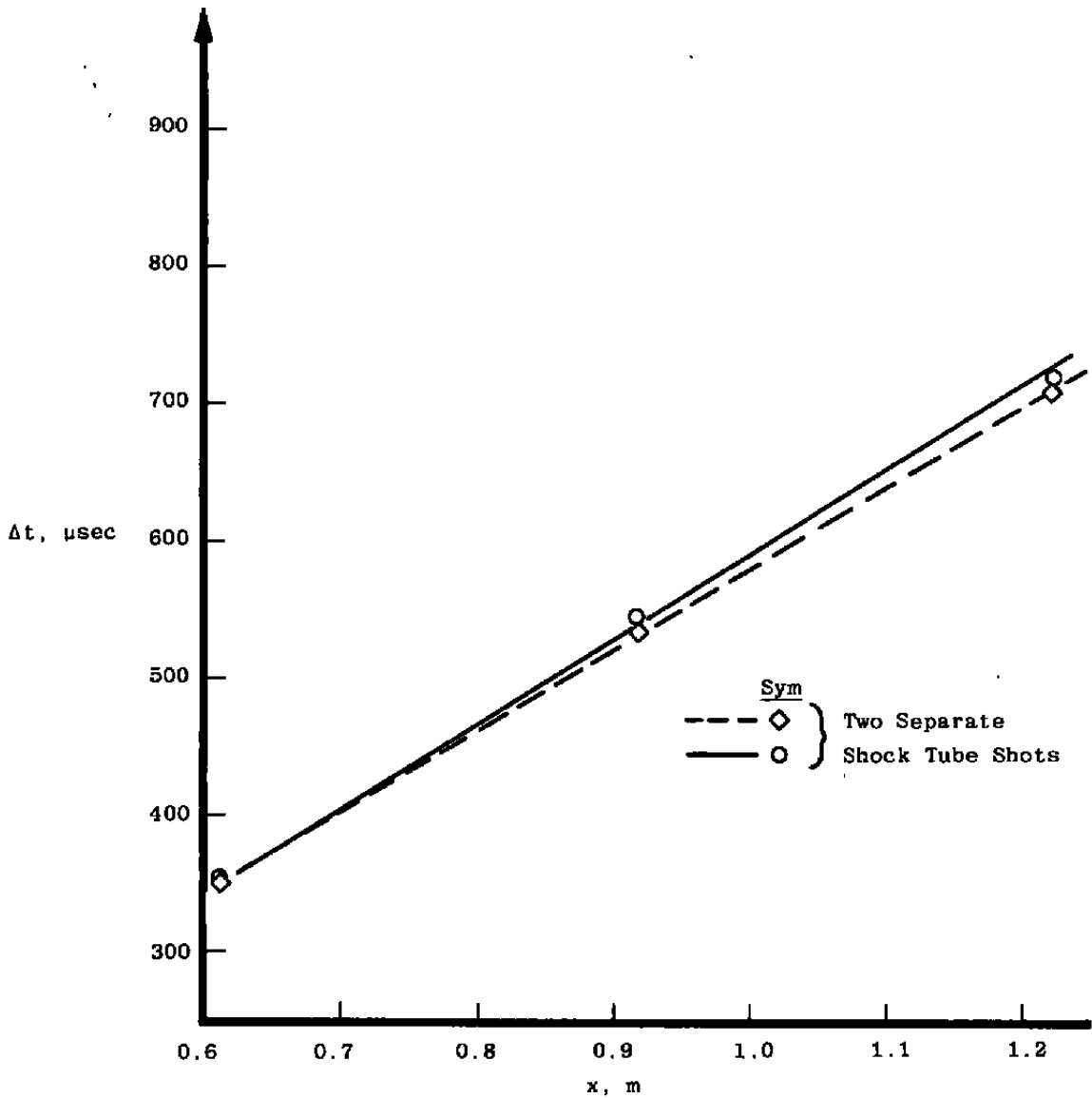


Figure 19. Shock front time - distance results.

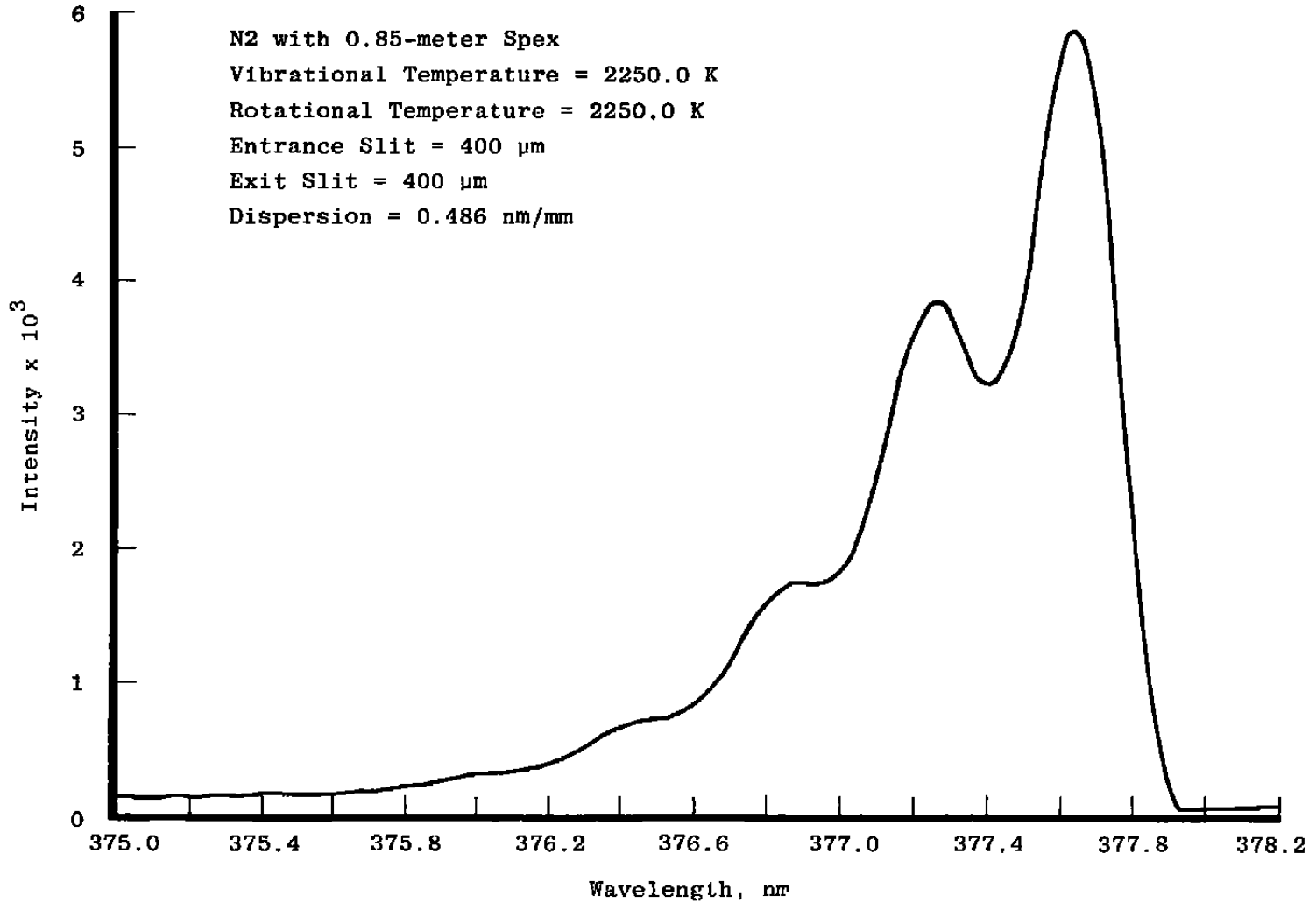


Figure 20. Raman spectral profile for N<sub>2</sub>.

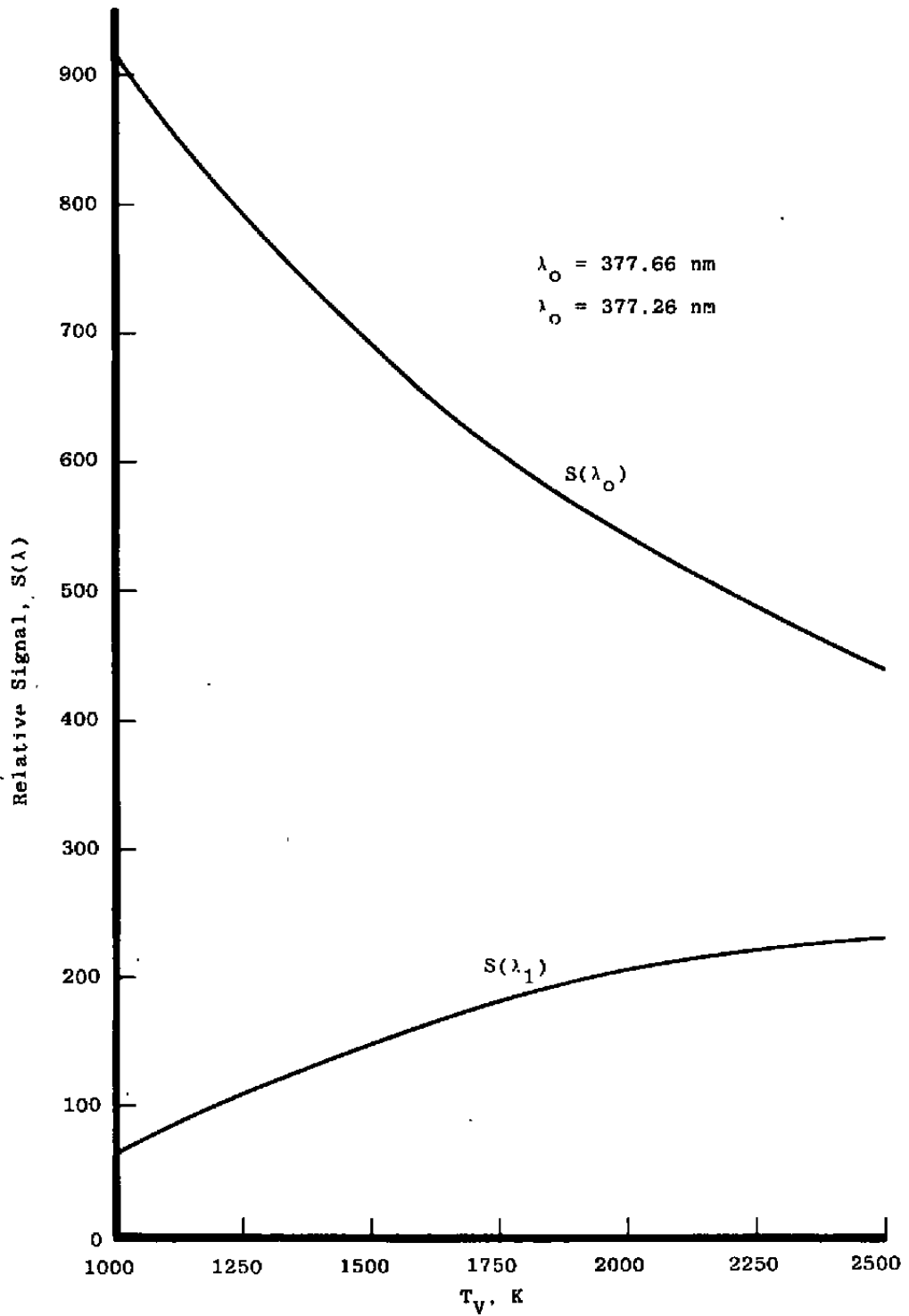


Figure 21. Variation of Raman signal levels with vibrational temperature  $T_v$ .

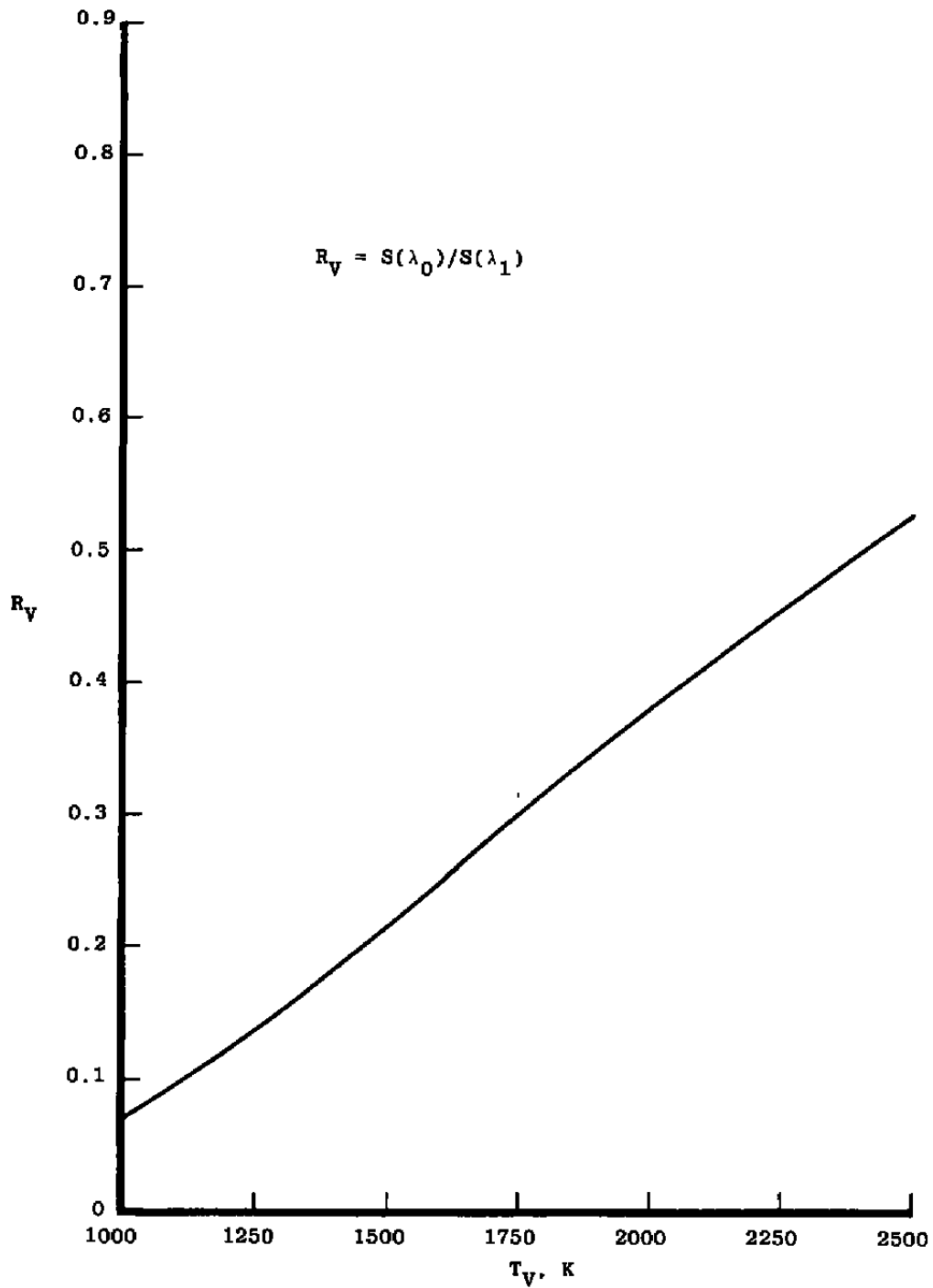


Figure 22. Ratio  $R_V$  of Raman signals versus  $T_V$ .

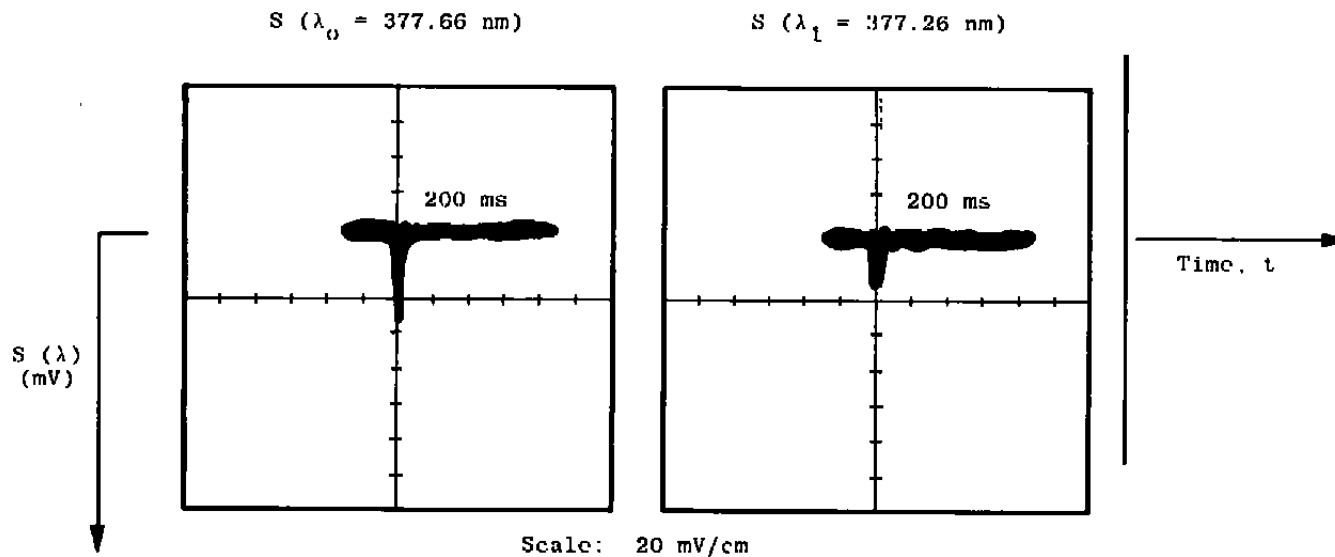


Figure 23. Oscilloscope traces of Raman signals  $S(\lambda_0)$  and  $S(\lambda_1)$ .

**Table 1. Conventional Instrumentation**

Type	Nominal Range	Parameter Measured
<b>Pressure Transducers</b> Tabor Tabor Kistler	$\leq 2,000$ psia (136 atm) $\leq 5$ psia (0.34 atm) $\leq 300$ psia (20 atm)	Driver Gas Pressure Test Gas Pressure Shocked Gas Pressure
<b>Low-Pressure Gauges</b> Thermal Conductivity (2) Wallace and Tiernan Ion Gauge	$\cong 10^{-2}$ torr $\leq 10^{-3}$ torr $\leq 100$ torr	Pumping Line Pressures Test Section Pressure Same
<b>Thermocouples</b> Copper - Constantan (2)	$\cong 250 - 300$ K	Driver and Driven Section Temperatures
<b>Thermistor</b>	$\cong 250 - 300$ K	Test Section Temperatures
<b>High-Pressure Gauges</b> Bourdon Bourdon	$\leq 2,000$ psia (136 atm) $\leq 600$ psia (41 atm)	Driver Gas Pressure Driven Gas Pressure

## NOMENCLATURE

$a_1$	Speed of sound in region 1
$D$	Diameter of shock tube
$d\sigma/d\Omega$	Differential cross section
$\tilde{E}_v$	Molar vibrational energy; $\tilde{E}_{ve}$ is the equilibrium value
$h$	Planck's constant
$\ell$	Length parameters
$\ell_m$	Maximum length of boundary-layer convected shocked gas
$M_i$	Mach number in region $i$
$\bar{M}_1$	Mean value of experimental measurements for incident Mach number
$n_i$	Number density in region $i$
$n_T$	Total number density
$P_i$	Pressure in region $i$
$P_o$	Power of laser
$R$	Universal gas constant
$R_v$	$S(\lambda_1)/S(\lambda_0)$
$(Re)_{s,t}$	Reynolds number of flow and transition, respectively
$S(\lambda)$	Raman signal at wavelength $\lambda$
$S/N$	Signal-to-noise ratio
$T, T_R, T_V$	Static, rotational, and vibrational temperatures, respectively

$\bar{T}_V$	Mean value of experimental measurements of $T_V$
$T_i$	Temperature in region $i$
$t$	Time
$t_\ell$	Laboratory time
$t_p$	Particle time
$t_p^{(0)}$	Ideal particle time
$t_a$	Laminar-turbulent boundary-layer transition time
$U_i$	Particle speed in region $i$ in shock wave coordinates
$V_i$	Particle speed in region $i$ in laboratory coordinates
$W_R$	Shock speed in reflected shock region
$W_S$	Incident shock speed
$x$	Position
$X_i$	Length parameters
$\gamma_i$	Specific heat ratio for gas in region $i$
$\eta$	Gas viscosity
$\lambda$	Wavelength; $\lambda_0$ and $\lambda_1$ , are Raman signal wavelengths and $\lambda_B$ is the wavelength for background radiation measurement
$\Phi$	Parameter representing $T$ , $n\gamma-1$ , and $p(\gamma-1)/\gamma$
$\nu_0$	Laser frequency
$\rho$	Gas mass density

$\theta_v$	Characteristic vibrational temperature of molecular vibrational mode
$\tau_i$	Defined by Eq. (8b)
$\tau_r$	Rotational relaxation time
$\tau_v$	Vibrational relaxation time
$\Delta\tau_i$	Observation time of incident shock wave
$\Delta\tau_i^+$	Maximum observation time of incident shock wave
$\Delta\tau_l$	Observation time for laminar boundary layer
$\Delta\tau_r$	Observation time in reflected shock region
$\Delta\tau_t$	Observation time for turbulent boundary layer
$\Delta\Omega$	Subtended solid angle